이학박사 학위논문

Study on Dzyaloshinskii-Moriya Interaction at Single Interface

단일 계면의 쟐로신스키-모리야 상호작용 연구

2023년 8월

서울대학교 대학원

물리천문학부

유 지 성

Study on Dzyaloshinskii-Moriya Interaction at Single Interface

단일 계면의 쟐로신스키-모리야 상호작용 연구

지도교수 최석봉

이 논문을 이학박사 학위논문으로 제출함

2023년 8월

서울대학교 대학원

물리천문학부

유 지 성

유지성의 이학박사 학위논문을 인준함

2023년 8월

위 원 장	박 윤	(인)
부위원장	최 석 봉	(인)
위 원	민 홍 기	(인)
위 원	박 철 환	(인)
위 원	홍 정 일	(인)

Study on Dzyaloshinskii-Moriya Interaction at Single Interface

Ji-Sung Yu

Supervised by
Professor Sug-Bong Choe

A Dissertation in Physics

Submitted to the Faculties of
Seoul National University
in Partial Fulfillment of the Requirements for the Degree of
Doctor of Philosophy

August 2023

Department of Physics and Astronomy
The Graduate College of Natural Sciences
Seoul National University

Abstract

Dzyaloshinskii-Moriya interaction (DMI) has emerged as a crucial element in the field of spintronics, playing a pivotal role in stabilizing chiral objects such as chiral domain-walls and skyrmions. Given its promising applications in next-generation memory-logic devices and its academic importance, extensive efforts have been dedicated to its study and exploration. However, the precise underlying mechanism of the emergence of DMI is still a subject of debate.

The widely accepted description for the emergence of DMI is due to the spin-orbit interaction of conduction electrons at interfaces, a phenomenon driven by structural inversion asymmetry (SIA). This suggests that DMI is essentially an interfacial effect, and a comprehensive understanding of the interface is vital to unravel its underlying mechanism.

However, the conventional experimental approach to investigate DMI is primarily based on systems with multiple interfaces, mainly due to the presence of a protection layer adjacent to the magnetic layer, which is utilized to prevent undesirable oxidation. As a result, the current experimental approach has a limitation in resolving the individual contribution of DMI at interfaces, potentially hindering a deeper understanding of DMI.

Here, we proposed a pioneering experimental approach that allows us to resolve the individual contributions of DMI at interfaces through direct observations of DMI at a single interface. This method provides a clearer and more comprehensive

investigation of DMI compared to the conventional approach, resulting in a deeper understanding of DMI.

In chapter 1, we introduce an overview of the historical descriptions of the DMI mechanism, delve into the basic physics of ferromagnetism in conventional systems exhibiting PMA, and the measurement scheme employed for investigating DMI. Throughout this chapter, we focus on the overall domain-wall (DW) dynamics in ultrathin ferromagnetic films with perpendicular magnetic anisotropy (PMA).

In chapter 2, we introduce a new experimental setup, called the in-vacuum MOKE system, which allows us to observe DMI at a single interface. The detection of DMI through the in-vacuum MOKE system builds upon the measurement scheme introduced in chapter 1. In this chapter, we primarily focus on setting up the new experimental setup and validating the DW dynamics in the single interface structure (Pt/Co) using this setup. The results obtained in this chapter mark a significant milestone in the study of single interface structures in relation to DW dynamics.

In chapter 3, we systematically investigate DMI in the Pt/Co single interface by varying the thickness of magnetic layer (Co). Our findings confirm the interfacial effect behavior of DMI. Furthermore, these results validate the reliability and accuracy of our experimental setup, enabling us to achieve precise control and detection over the thickness, even down to sub-atomic scale thickness.

In chapter 4, following a similar approach to the investigation in chapter 3, we systematically investigate DMI in the Pt/Co single interface, but this time by varying the thickness of non-magnetic layer (Pt). Interestingly, a pronounced dependence of

DMI on the non-magnetic layer thickness is observed, in contrast to theoretical expectation. Additionally, systematic examination of X-ray diffraction (XRD) reveals a correlation between DMI and lattice constant of Pt. This finding is further validated through first-principles study. Furthermore, by utilizing the clearly revealed correlation in conventional systems, we develop a method for chirality manipulation. By thoroughly investigating the thickness dependence of both the magnetic layer and non-magnetic layer at the Pt/Co single interface in chapters 3 and 4, we achieve a comprehensive understanding of DMI at the Pt/Co interface.

In chapter 5, based on the enhanced understanding of DMI at the Pt/Co interface established previous chapters, we conduct a systematic investigation into the emergence of DMI for various materials. This investigation utilizes the state-of-the-art capabilities of the in-vacuum system. In this experimental study, we systematically explore DMI in Pt/Co/X, where X represents a selection of various materials, including Al, Cu, Nb, Pd, Hf, and Ta. The exploration is carried out through step-by-step deposition of these materials onto Co with a sub-atomic scale layer thickness. Through this well-controlled investigation, we quantify layer-resolved contributions of DMI for various materials. Furthermore, we unveil the existence of a universal length of interface, which plays an essential role in the emergence of DMI. These findings shed light on the interfacial characteristics of DMI and provide insights into the underlying nature of its emergence.

In chapter 6, we introduce a new measurement scheme specifically designed for investigating DMI in the case of weak PMA. In the previous chapters, the investigation of DMI was conducted under the condition of strong PMA, where clear DW motion was observed. This facilitated accurate measurement of the DW speed for quantifying DMI. However, in the case of weak PMA, detecting the DW motion becomes challenging, which consequently hinders the precise measurement of DMI. In this chapter, we propose a new method for quantifying DMI based on DW roughness measurement. This measurement scheme serves as a solution to the difficulties encountered in DMI measurement based on DW motion in weak PMA systems.

In chapter 7, the conclusion, and the outlook of the results presented in this thesis are provided. The main findings of this thesis were achieved through observations of DMI at the Co/X single interface. This pioneering result significantly advances the field of DMI by providing clear detection and in-depth analysis of the phenomenon.

Key words: Dzyaloshinskii-Moriya interaction, interface, domain-wall, perpendicular magnetic anisotropy, magneto-optical Kerr effect, chirality

Student number: 2017-20880

Table of Contents

List of Figures

Chapter 1

Introduction

In this chapter, we begin with a concise historical overview of the development of the DMI mechanism. Subsequently, we delve into the fundamental physics of ferromagnetism in conventional systems exhibiting PMA. Furthermore, we present an analysis of domain-wall (DW) dynamics and introduce a measurement scheme for quantifying DMI. This measurement scheme serves as the foundation for studying DMI at a single interface.

1.1 Dzyaloshinskii-Moriya Interaction

Dzyaloshinskii-Moriya interaction (DMI) is an asymmetric exchange interaction that prefers the chiral spin ordering. Its energy form is given as $E_{\mathrm{DMI}} = -\vec{D} \cdot (\vec{S}_1 \times \vec{S}_2)$, where $\vec{D}$ is the DMI vector, and $\vec{S}_1$, and $\vec{S}_2$ are two spins involved. Figure 1.1 illustrates a schematic of the atomic geometry of DMI. Due to its chiral nature, DMI depends on the atomic geometry in conjunction with the material. Consequently, for the same material, the chirality is reversed when the positions of the materials are reversed. Therefore, in a symmetric structure, the DMI becomes zero, indicating that DMI is driven by structural inversion asymmetry (SIA).

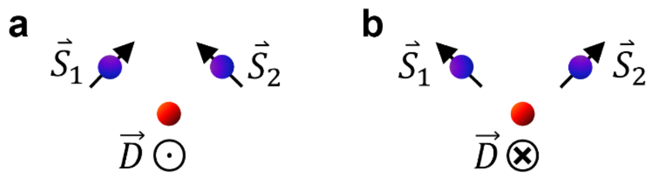

Figure 1.1 Schematic of the atomic geometry of DMI. a, Counterclockwise chirality. b, Clockwise chirality.

Historically, the concept of DMI was first proposed phenomenologically by I. Dzyaloshinskii in 1958 [1], and later, T. Moriya demonstrated it theoretically within the scope of the super-exchange interaction model in 1960 [2]. Later, in 1980, A. Fert and P.M Levy proposed a mechanism related to spin-orbit scattering, which explained the chiral spin structures around impurity in CuMn spin glasses [3]. Subsequently, the Rashba mechanism was also proposed [4], further expanding the understanding of

DMI. As research progressed, additional mechanisms have been proposed to explain DMI, including Doppler shift description [5], the Berry phase theory [6], and other approaches [7-9]. These early works laid the foundation for the understanding of DMI. Though the precise mechanism of DMI is under debate, the general understanding of DMI is that it is an interfacial phenomenon that arises due to spin-orbit interaction at the interface.

1.2 Conventional ferromagnetic systems exhibiting PMA

In this thesis, the primary focus is on the study of ultra-thin ferromagnetic films with PMA. Before delving into the investigation of single interface structures, the properties of conventional ferromagnetic systems are explored.

The conventional films consist of layered structures, where buffer (mainly Ta) / non-magnet (NM1, mainly Pt) / ferromagnet (FM, mainly Co) / non-magnet (NM2) layers are sequentially deposited on Si/SiO_2 substrates, as illustrated in Fig. 1.1a. Each layer has a thickness ranging from sub-nanometer to a few nanometers, deposited by conventional DC magnetron sputtering. The chamber's base pressure is maintained at a low value of 10^{-8} Torr, and the deposition process is conducted under an Ar atmosphere at 2 mTorr. To ensure systematic control of each ultra-thin layer, deposition rates are set to approximately 0.2 Å/s using low power. The key characteristic of this film is its perpendicular magnetic anisotropy (PMA), where the easy axis aligns with the film's normal direction. The anisotropy field H_K and saturation magnetization M_S of the film are about $0.5 \sim 2.5$ T and around 10^6 A/m, respectively.

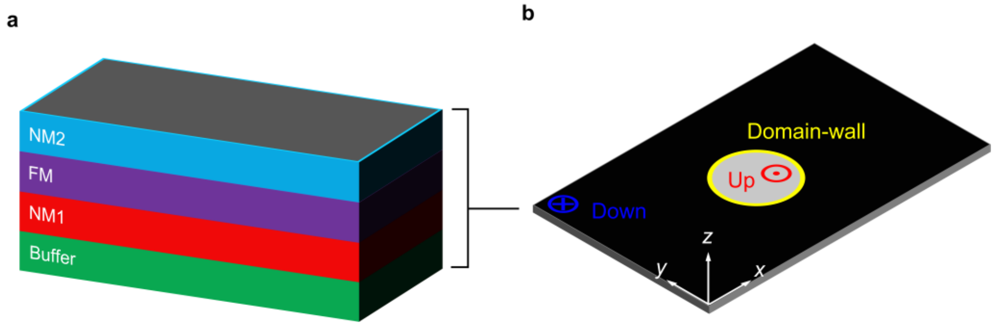

Figure 1.2 Schematic of conventional system. a, diagram of layered structure. b, magnetic domains, and domain-walls (DWs) on the film.

1.3 Magnetic domains and DWs

Magnetic domains are regions where the magnetization is uniformly aligned in a certain direction. Due to the strong PMA in the ferromagnetic films, two types of magnetic domains can exist: up-domains, where the magnetization is uniformly aligned parallel to the film normal, and down-domains, where the magnetization is uniformly aligned anti-parallel to the film normal, as illustrated in Fig. 1.2b. Magnetic domain-walls (DWs) are boundaries between magnetic domains, represented by yellow curves in Fig. 1.2b. Inside the DWs, the magnetization has a gradual configuration from the down-state to the up-state (or vice versa), as illustrated in Fig. 1.3. This magnetization configuration extends over a finite distance, known as the DW width, which is determined by intrinsic parameters of material. The typical value of DW width is ranges from a few nanometers to a few tens of nanometers in PMA systems.

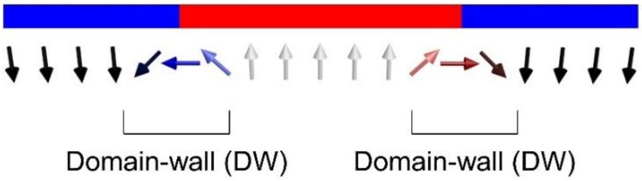

Figure 1.3 Schematic diagram of magnetization configuration inside DWs.

The magnetic domains can be expanded or shrink by the application of an external magnetic field. When an external out-of-plane magnetic field is applied, the magnetic domains with magnetization aligned parallel to the external field direction expand to reduce Zeeman energy. Conversely, the domains with magnetization aligned anti-parallel to the external field direction shrink. Through careful observation and analysis of the response of the magnetic domains to the external magnetic field, the dynamics of DWs are primarily investigated. Understanding these dynamics allows for the exploration of the intrinsic properties of the systems under study.

1.4 DW dynamics in creep regime

The motion of DW in ferromagnetic thin films provides an example of a moving elastic interface in a weakly disordered medium. Depending on the relative strength of the driving force f in comparison to the depinning force f_{dep}, the DW dynamics can be categorized into three different regimes: [10] (i) the flow regime, (ii) the depinning regime, and (iii) the creep regime.

(i) In the flow regime, when $f \gg f_{\mathrm{dep}}$, the DW motion is characterized by a dissipative viscous flow motion, where disorder plays a negligible role. In this regime, the DW speed v_{DW} is directly proportional to the applied driving force f.

(ii) In the depinning regime, when $f \sim f_{\mathrm{dep}}$, the DW motion experiences a transition between the creep regime and the flow regime. In this regime, the DW starts to depin from the energy landscape of the disorder.

(iii) In the creep regime, when $f \ll f_{\mathrm{dep}}$, the DW motion is predominantly governed by thermal activation, and the DW stochastically depins by overcoming the pinning potential barriers.

In this thesis, the DW dynamics in the creep regime is mainly studied due to its academic significance as well as its experimental feasibility and simplicity. The unique advantages of investigating DW dynamics in the creep regime provide a foundation for further exploration and utilization in studying the single interface structure. Therefore, understanding the comprehensive characteristics of DW motion in the creep regime provides insights into the behavior of single interface structures.

Returning to the main point, in the creep regime, v_{DW} is governed by the creep scaling law [10-11], which is expressed as:

$$v_{\mathrm{DW}} = v_0 \exp\left[-\alpha H_z^{-\mu}\right], \tag{1.1}$$

where v_0 is the characteristic velocity, α is the creep scaling constant, and μ is the creep exponent $(= 1/4)$ in our systems. The H_z is an external out-of-plane magnetic field, which acts as the driving force f in our systems. The creep scaling law is well confirmed in conventional systems, as shown in Fig. 1.4.

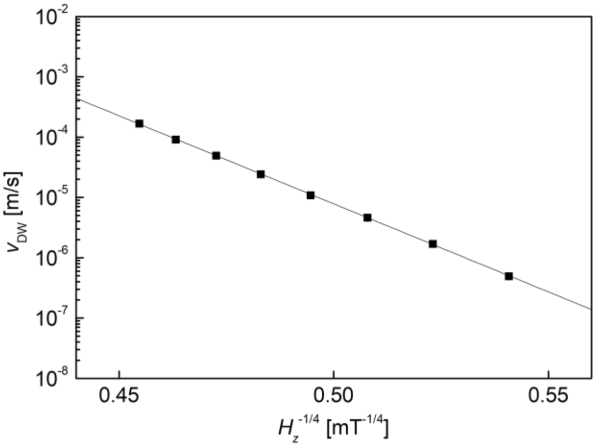

Figure 1.4 Plot of v_{DW} as a function of $H_z^{-\mu}$ with $\mu = 1/4$. The solid line is the best fitting of the creep scaling law.

Furthermore, through a careful analysis of the creep scaling law, we can also determine an important property of the systems, the effective magnetic layer thickness [12]. When dealing with ultra-thin ferromagnetic films, precise control of the magnetic layer thickness is of utmost importance, as the properties of the system are highly sensitive to the magnetic layer thickness in such ultra-thin films. A comprehensive examination of the creep scaling constant α involves its original definition as $\alpha \equiv U_{\mathrm{C}}(H_{\mathrm{crit}})^{1/4}/k_{\mathrm{B}}T$, where U_{C} is the scaling energy constant for the effective DW pinning energy barrier, and H_{crit} is the critical field required to move the DW at zero temperature [11-12]. These parameters are interrelated as follows: $U_{\mathrm{C}} \propto \left(f_{\mathrm{pin}}^{2} \varepsilon_{\mathrm{el}} \xi^{5} n_{i}\right)^{1/3}$ and $H_{\mathrm{crit}} \propto \left(f_{\mathrm{pin}}^{4} \varepsilon_{\mathrm{el}}^{-1} \xi n_{i}^{2}\right)^{1/3} t_{\mathrm{Co}}^{-1}$, where f_{pin} is the local pinning force, $\varepsilon_{\mathrm{el}}$ is the Bloch-type DW energy density per unit length, ξ is the characteristic length of the disorder potential, and n_{i} is the surface density of the pinning centers, and t_{Co} is the magnetic layer (Co) thickness. The parameters ξ and n_{i} are independent of t_{Co}, whereas f_{pin} and $\varepsilon_{\mathrm{el}}$ are linearly proportional to t_{Co}. By summarizing all these t_{Co} dependence relationships, we can finally obtain $U_{\mathrm{C}} \propto (t_{\mathrm{Co}})^{1}$ and $H_{\mathrm{crit}} \propto (t_{\mathrm{Co}})^{0}$, leading to the scaling relationship [12].

$$\alpha \propto t_{\mathrm{Co}} \tag{1.2}$$

This relationship indicates that the creep scaling constant α can be utilized for sensing the magnetic layer thickness, and it is validated in Pt/Co/Pt and Pt/Co/TiO_2/Pt systems, for effective Co thickness $t_{\mathrm{Co}} - t_{\mathrm{Dead}}$, as shown in Fig. 1.5. [12]

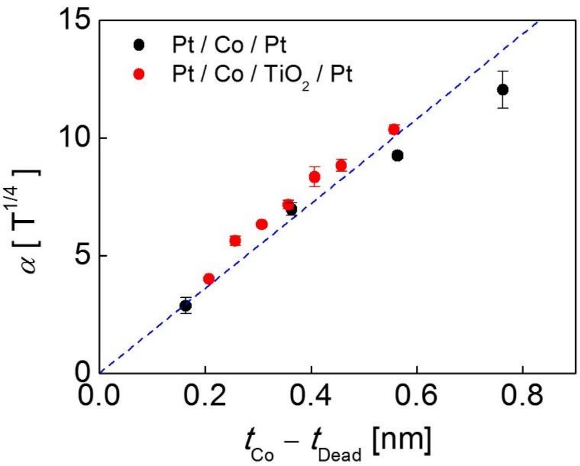

Figure 1.5 Plot of creep scaling constant α with respect to effective Co thickness

$t_{Co} - t_{Dead}$ for the series of films of Pt/Co/Pt (black) and Pt/Co/TiO_2/Pt (red). The blue dashed line guides the eye for the linear relationship.

1.5 Types of chiral DW induced by DMI

As mentioned in chapter 1.1, the Dzyaloshinskii-Moriya interaction (DMI) prefers chiral spin ordering, and the chirality of DW is manipulated by interfacial DMI in low-dimensional magnetic systems [13-15]. Figure 1.6 illustrates three distinct chirality of DW: left Néel (counterclockwise, CCW) on the left side, Bloch in the middle, and right Néel (clockwise, CW) on the right side in the figure. In these systems, DMI acts as an effective magnetic field, H_{DMI} within the DW. The direction of H_{DMI} determines the types of DW, with a negative (positive) direction leading to left Néel (right Néel) DW, respectively. In the absence of DMI, the DW chirality prefers Bloch DW to reduce the magnetostatic energy.

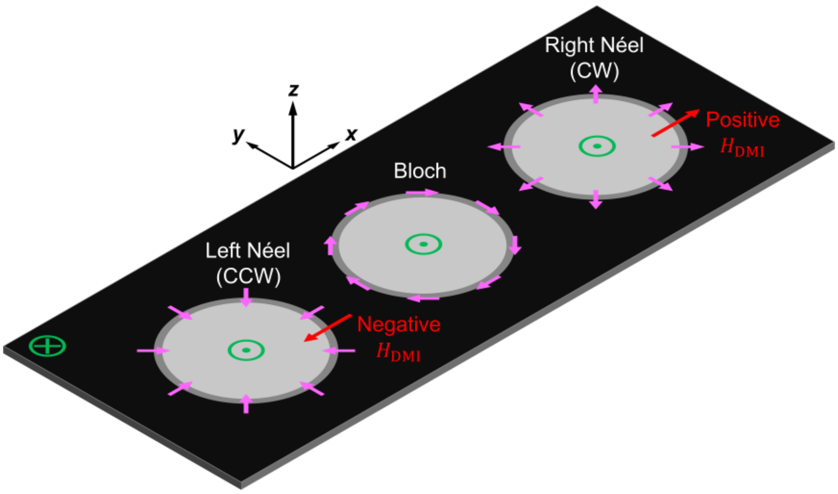

Figure 1.6 Graphic illustration of three distinct chirality of DW. Each DW type

is denoted in the figure. The green symbols indicate the magnetization direction of domains. The pink arrows indicate the magnetization direction of the DW. The red arrows indicate the presence of H_{DMI}.

1.6 Asymmetric DW speed scheme for DMI measurement

In general, the DW energy is influenced by various magnetic properties, including magnetic anisotropy, exchange stiffness, and DMI. In magnetic systems with strong PMA, the DW energy density σ_{DW} under the application of an external in-plane magnetic field H_x is given by

$$\sigma_{\mathrm{DW}}(H_x) = \begin{cases} \sigma_0 - \dfrac{\pi^2 \lambda M_{\mathrm{S}}^2}{8K_{\mathrm{D}}}(H_x + H_{\mathrm{DMI}})^2 & \text{for } |H_x + H_{\mathrm{DMI}}| < \dfrac{4K_{\mathrm{D}}}{\pi M_{\mathrm{S}}}, \\ \sigma_0 + 2K_{\mathrm{D}}\lambda - \pi\lambda M_{\mathrm{S}}|H_x + H_{\mathrm{DMI}}| & \text{otherwise} \end{cases} \quad (1.3)$$

where σ_0 is the Bloch-type domain-wall energy density, K_{D} is the domain-wall anisotropy energy density, λ is the domain-wall width, and H_{DMI} is the effective magnetic field induced by DMI [14-15].

The DW speed v_{DW} is determined by the modification of the DW energy density $\sigma_{\mathrm{DW}}(H_x)$ due to the DW creep criticality [11, 14-15] as given by

$$v_{\mathrm{DW}}(H_x) = v_0 \exp\left[-\alpha_0 \left(\frac{\sigma_{\mathrm{DW}}(H_x)}{\sigma_0}\right)^{1/4} {H_z}^{-1/4}\right], \quad (1.4)$$

where v_0 is the characteristic speed, α_0 is the creep-scaling constant of the Bloch DW, and H_z is the external out-of-plane magnetic field.

Figure 1.7 illustrates the typical functional shapes of $\sigma_{\mathrm{DW}}(H_x)$ and $v_{\mathrm{DW}}(H_x)$ with respect to H_x, while keeping H_z constant. The plot clearly shows that both $\sigma_{\mathrm{DW}}(H_x)$ and $v_{\mathrm{DW}}(H_x)$ exhibit symmetric variations with respect to a symmetric axis (green vertical line). According to Eq. (1.3), the position of this symmetric axis corresponds to the condition $H_x = -H_{\mathrm{DMI}}$.

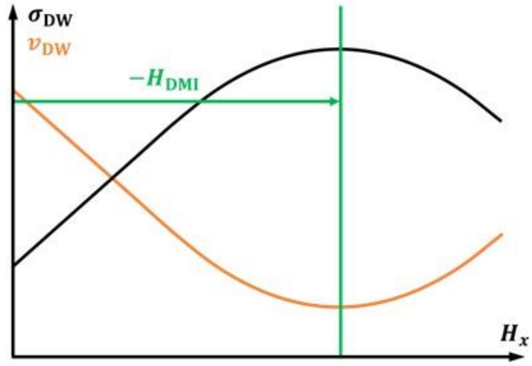

Figure 1.7 Schematic drawings of Eqs. (1.3) and (1.4) with respect to H_x. The green vertical line indicates the symmetric axis, corresponding to $-H_{\mathrm{DMI}}$.

Using this scheme, the measurement of DMI for each type of chiral systems is conducted, as shown in Fig. 1.8. The figure shows the plot of v_{DW} with respect to H_x under the application of a constant out-of-plane magnetic field H_z. The position of its symmetric axis exhibits positive (Fig. 1.8a), around zero (Fig. 1.8b), and negative (Fig. 1.8c), corresponding to the negative Right Néel (CW chirality), Bloch, and Left Néel (CCW chirality) DWs, respectively. Therefore, this measurement scheme can unambiguously determine the strength of DMI as well as DW chirality from the position of the symmetric axis.

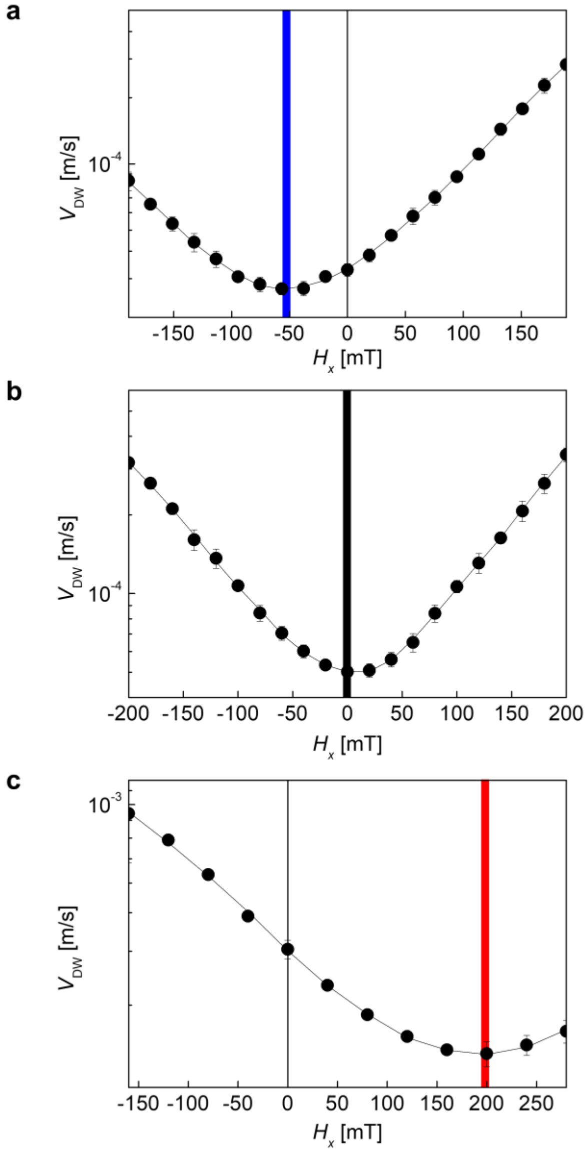

Figure 1.8 Plot of v_{DW} with respect to H_x for different DW chirality. a, CW, b, Bloch, and c, CCW. The colored vertical line indicates the positions of their respective symmetric axis.

Chapter 2

Experimental setup

In this chapter, we initially address the challenges of the current measurement system used for investigating interfacial phenomena. Subsequently, we present the development of a conventional magneto-optical Kerr effect (MOKE) microscopy system equipped with 2-axis electromagnets, which enables in-vacuum compatible measurements. This improved setup is specifically designed to overcome the raised challenges. With the implementation of this improved setup, the characteristics of single interface is clearly investigated through a careful analysis of DW dynamics.

2.1 Branch of interfacial phenomena and challenges

Interfacial phenomena arise at interface due to interactions associated with structural inversion asymmetry (SIA) and spin-orbit interaction. These phenomena include PMA [16], Rashba effect [17-18], spin-Hall effect [19-20], DMI [1-9], and other effects observed in conventional magnetic systems.

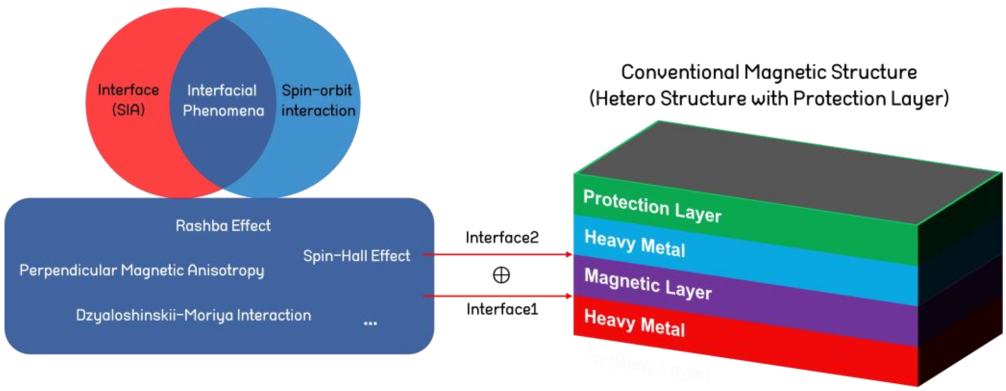

Figure 2.1 Schematic of interfacial phenomena and conventional magnetic structures.

The conventional methodology for investigating these interfacial phenomena is mainly conducted using heterostructures with a protection layer. This protection layer prevents undesired oxidation, enabling systematic investigations of the phenomena.

However, the presence of these additional layers adjacent to the magnetic layer inevitably leads to the formation of multiple interfaces, making it challenging to isolate and observe the desired phenomena at the specific interface of interest. As a consequence, the observed interfacial phenomena are a result of the combination of effects from multiple interfaces, complicating the interpretation of experimental results. This interference from multiple interfaces hinders the clear understanding and identification of the individual contributions of each interfacial phenomenon, as depicted in Fig. 2.1.

Therefore, in order to study the interfacial DMI more accurately, it becomes imperative to resolve the individual contributions at the interfaces. By isolating the specific interface of interest and eliminating interference from other interfaces, we can achieve a clearer understanding of the interfacial DMI and its distinct effects on the system.

2.2 Approach for isolating single interface

To overcome the challenges posed by multiple interfaces and investigate specific interfacial phenomena more precisely, a novel approach is proposed: constructing a magnetic system with a single interface and conducting measurements under carefully controlled vacuum conditions to prevent undesired oxidations and ensure systematic investigations, as illustrated in Fig. 2.2.

By designing a magnetic structure with a well-defined single interface, we can focus solely on the interactions and phenomena occurring at that specific interface. This eliminates the complexities introduced by multiple interfaces and allows for a more accurate interpretation of experimental results.

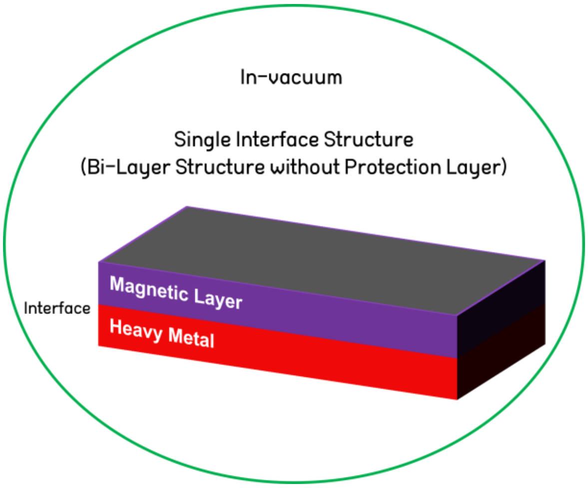

Figure 2.2 Schematic of isolating single interface.

2.3 Magneto-optical Kerr effect (MOKE)

Magnetic DW dynamics has garnered significant attention in the field of magnetism, attracting both academic interest [10-15] and showing promising potential for practical applications in next-generation memory and logic devices, such as magnetic racetrack [21-22] and bubblecade [23] memory. Consequently, the precise observation and understanding of DW dynamics hold paramount importance.

Hence, the utilization of magneto-optical Kerr effect (MOKE) offers ideal platform for observing these DW dynamics, and its effectiveness has been validated in various magnetic systems [10-15]. Figure 2.3 illustrates the working principles of MOKE in distinguishing two different domains. The Kerr rotation, R_{K} is generally depending on the polarization of the lights and magnetization states, expressed as $R_{\mathrm{K}} \propto m \times E$, where m is the magnetization, E is the polarization of lights.

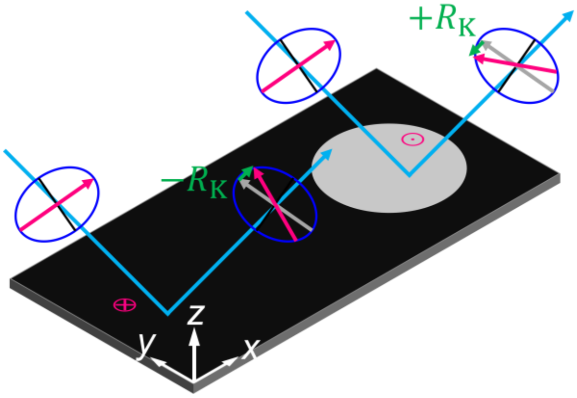

Figure 2.3 Schematic diagram of MOKE. The polarization of the lights (pink arrows) reflected from up-domain (grey) and down-domain (black) regions, experiencing different Kerr rotations, R_K, depending on the magnetization state of the domains.

2.4 In-vacuum MOKE system

Our in-vacuum DMI characterization system adopts a measurement scheme based on the asymmetric domain-wall speed [14]. In this scheme, the domain expansion patterns under the application of a magnetic field are monitored using a magneto-optical Kerr effect (MOKE) microscope equipped with two-axis electromagnets. By analyzing the observed domain expansion patterns, we can measure the domain-wall speed accurately. The advantage of this measurement scheme is that it allows us to observe domain expansion patterns in continuous films without the need for any specific structures, making it compatible with the in-vacuum measurement system. Furthermore, the MOKE signal exhibits high sensitivity to ultrathin films, even below the thickness of a single atomic layer, making it suitable for studying the initial formation of interfaces with subtle changes at the atomic level. Considering these factors, we have chosen the asymmetric domain-wall speed scheme for our in-vacuum iDMI characterization system.

Figure 2.4 presents the layout of our in-vacuum DMI characterization system, which comprises four main components:

1) The deposition chamber, a conventional DC magnetron sputtering system, includes a heater for precise temperature control during the deposition process. After the sample is deposited inside the deposition chamber, it is transferred via a transfer tube and a motorized XYZ stage to the measurement position located in front of the window at the end of the characterization chamber.

2) The characterization chamber, where the measurements are performed, houses the sample at the measurement position, precisely centered between the two-axis electromagnets and at the focal plane of the magneto-optical Kerr effect (MOKE) microscope.

3) The two-axis electromagnets consist of an in-plane and an out-of-plane electromagnet, accurately aligned to their common center at the measurement position. To maintain the desired vacuum level and prevent any temperature increase inside the chamber, the electromagnets are situated outside the chamber.

4) The MOKE microscope is equipped with a long-working-distance objective lens, allowing for observation of the samples at the measurement position inside the

chamber through the window. The illumination light is provided by a metal-halide lamp, which exhibits maximum intensity peaks at the wavelengths of 365 nm and 425 nm. The spatial resolution, defined by the Rayleigh criterion, as $0.61\lambda/\mathrm{NA}$, is approximately 1 μm, with a numerical aperture of 0.25.

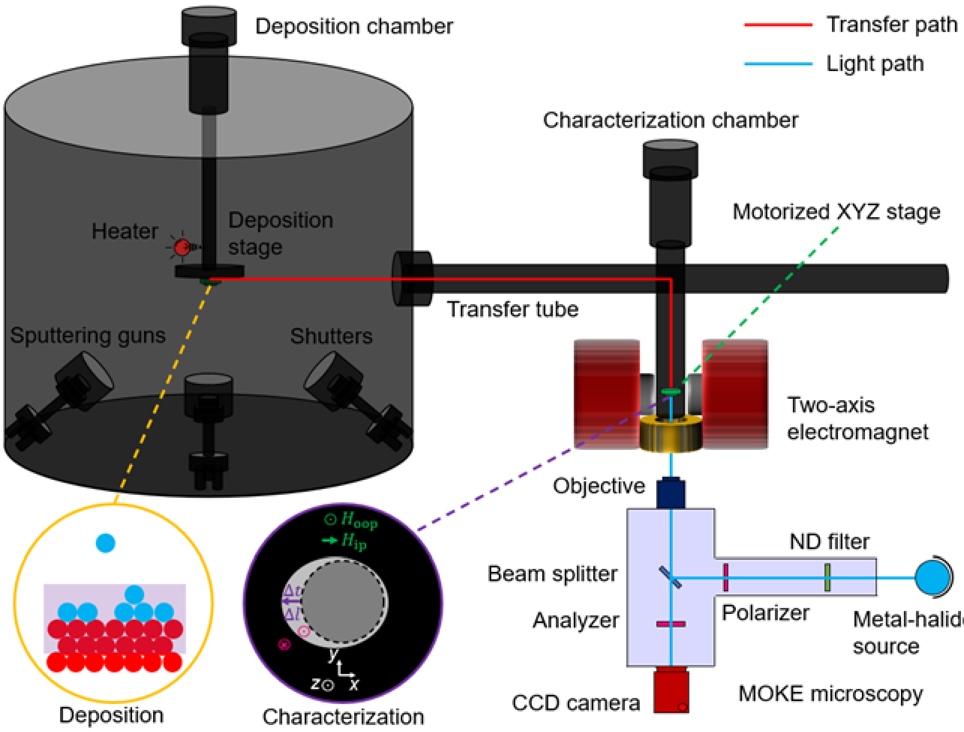

Figure 2.4 Schematics of experimental setup of in-vacuum MOKE system. The system consists of the deposition chamber, characterization chamber, MOKE microscope, and motorized XYZ stage. The red and blue solid lines indicate the sample transfer path and light path, respectively.

2.5 Verification of DW creep in single interface systems

To investigate the DMI based on the asymmetric DW speed scheme [14], it is crucial to verify the validity of DW creep dynamics in single interface systems. In this study, a series of 5.0-nm Ta/2.5-nm Pt/t_{Co}-nm Co films were fabricated on Si/100-nm SiO_2 substrates using dc magnetron sputtering. The deposition temperature was maintained at ~320K to optimize the magnetic signal in the system. The Co layer thickness, denoted as t_{Co}, was varied from 0.5 to 1.4 nm with a 0.1-nm increment. Such a small variation in the Co layer thickness affects the fractional coverage at the interface, influencing the interfacial magnetic properties. After deposition, the films were transferred to the measurement chamber using a transfer tube and motorized 3-direction XYZ stage. Subsequently, the magnetic properties were measured in-vacuum using an in-vacuum magneto-optical Kerr effect (MOKE) microscope to observe the magnetization dynamics.

Figure 2.5 presents the MOKE image of domains in the Pt/Co single interface system, showing clear circular domains, indicative of strong PMA.

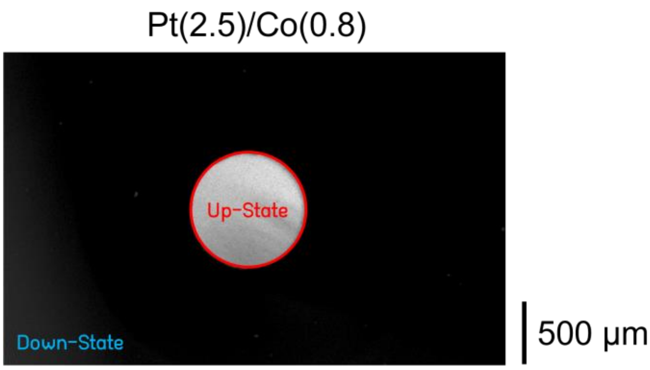

Figure 2.5 MOKE image of domains in Pt(2.5)/Co(0.8). The grey (black) region indicates up (down) domain.

From these clear circular magnetic domains, the domain wall speed v_{DW} was measured by analyzing subsequent images of domain expansion under the application of an external magnetic field H. Figure 2.6 shows the creep-scaling plot of v_{DW} as a function of $H^{-1/4}$ for films with different t_{Co} as denoted in the plot. The clear linear dependencies in the plot confirm that the current system is governed by the creep-scaling law, expressed by

$$v_{\mathrm{DW}} = v_0 \exp[-\alpha H^{-\mu}], \tag{2.1}$$

where v_0, α, and μ are the characteristic velocity, the creep-scaling constant, and the creep exponent (=1/4 in our system) respectively [10-11].

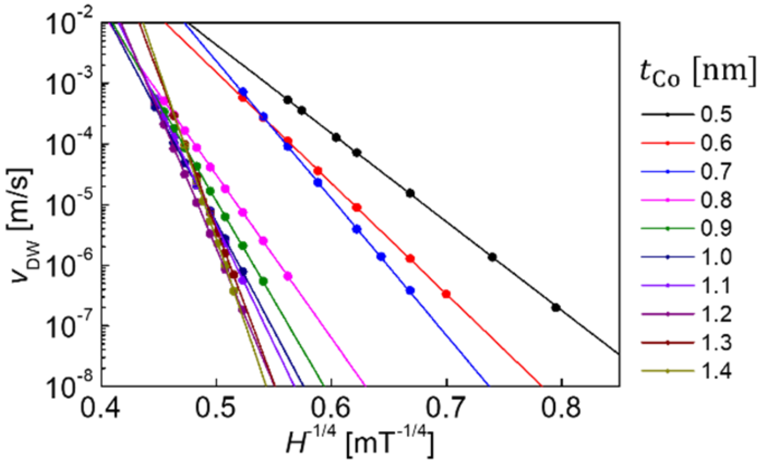

Figure 2.6 Plot of v_{DW} as a function of $H^{-1/4}$ from $t_{\mathrm{Co}} = 0.5$ nm to $t_{\mathrm{Co}} = 1.4$ nm. The solid lines indicate the best fitting with the creep-scaling law.

Based on the best linear fitting of the creep-scaling law, the relationship between α and t_{Co} can be determined, as shown in Fig. 2.7. The results unequivocally demonstrate a linear dependence between α and t_{Co}, as discussed in chapter 1.4.

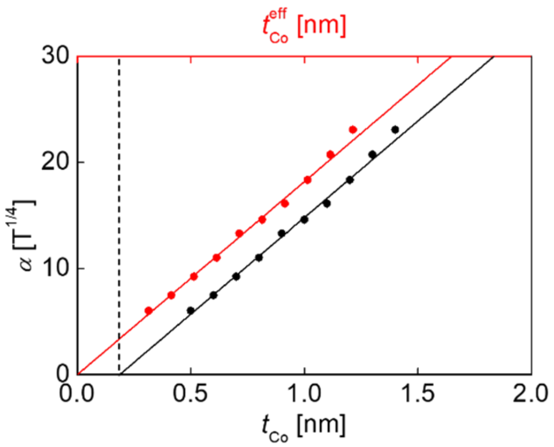

Figure 2.7 Plot of α with respect to t_{Co} (black) and $t_{\mathrm{Co}}^{\mathrm{eff}}$ (red) respectively. The solid lines indicate the best linear fitting, and the vertical black dashed line indicates the intercept to the abscissa.

These results provide strong evidence for the validity of DW creep in single interface systems, and they demonstrate that our experimental setup is highly sensitive to sub-atomic coverage. This sensitivity is essential for observing and studying interfacial phenomena accurately.

Chapter 3

Magnetic layer thickness dependence of DMI

In this chapter, we explore the impact of magnetic layer thickness on the DMI in the Pt/Co single interface system. By systematically varying the Co layer thickness, we investigate the behavior of interfacial DMI. Our results present compelling evidence supporting the interfacial nature of DMI and provide a testament to the reliability and precision of our experimental setup. Notably, our setup allows for precise control and detection of magnetic layer thickness, even down to the sub-atomic scale.

3.1 Background

Interfacial Dzyaloshinskii-Moriya interaction (DMI) emerges as a consequence of structural inversion asymmetry (SIA), particularly in low-dimensional magnetic systems. The significance of DMI is closely related to its association with chirality, as recent studies have revealed its crucial role in the formation of chiral magnetic objects [13-14, 24-25]. Therefore, establishing a general understanding of DMI, independent of specific material dependencies, is crucial before delving into more detailed investigations.

A recent study [26] has provided evidence for the magnetic layer thickness dependence of DMI in Co and CoFeB based magnetic systems. The findings indicate that DMI decreases with an increase in the thickness of the magnetic layer, supporting the interfacial nature of DMI. Additionally, a thorough investigation of ultra-thin magnetic layer thickness dependence has led to the identification of a critical thickness in Co based magnetic systems [27]. Moreover, it has been suggested that the thickness dependence of DMI originates from a linear relationship between the Heisenberg exchange interaction and DMI in NiFe based magnetic systems [28].

In this study, we investigate the magnetic layer thickness dependence of DMI in Pt/Co single interface systems, allowing us to isolate and analyze the DMI behavior without any potential mutual interference between interfaces. This approach offers a clear and focused examination of the thickness dependence of DMI, shedding light on the interfacial phenomena in these systems.

3.2 Sample fabrication

In this study, a series of 5.0-nm Ta/2.5-nm Pt/t_{Co}-nm Co films were fabricated on Si/100-nm SiO_2 substrates using dc magnetron sputtering. The deposition temperature was maintained at ~320K to optimize the magnetic signal in our system. We systematically varied the thickness of the Co layer t_{Co} from 0.5 nm to 1.4 nm with a 0.05-nm increment. This small variation in the Co layer thickness allowed us to study the influence of the fractional coverage at the interface on the interfacial magnetic properties, particularly the DMI. To investigate the interfacial DMI, the films were transferred to the measurement chamber through a transfer tube, using a motorized 3-direction XYZ stage for precise positioning. The in-vacuum DMI measurements were performed using a MOKE microscope, enabling the observation and analysis of the asymmetric DW speed. Figure 3.1 illustrates the schematic of the sample structures used in this study.

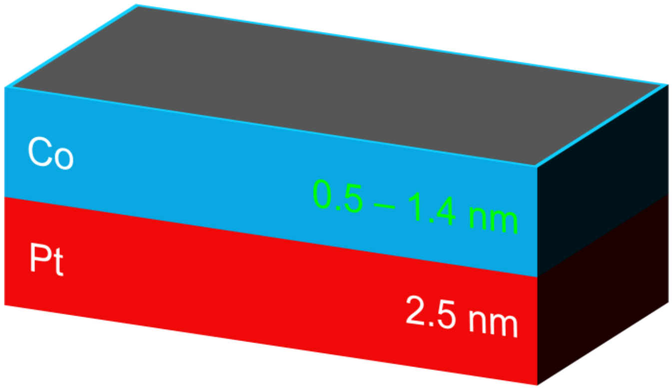

Figure 3.1 Schematic of sample structures of Pt/Co.

3.3 Magnetic layer thickness dependence of DMI

Figure 3.2 shows the plot of H_{DMI} with respect to t_{Co}. The experimental data show a clear trend of H_{DMI} smoothly decreasing as t_{Co} increases, which strongly suggests an interfacial behavior of the DMI [29]. Furthermore, these findings highlight the sensitivity of DMI to changes in t_{Co} and show that our experimental setup allows us to precisely resolve and detect sub-atomic scale thickness variations in the Co layer.

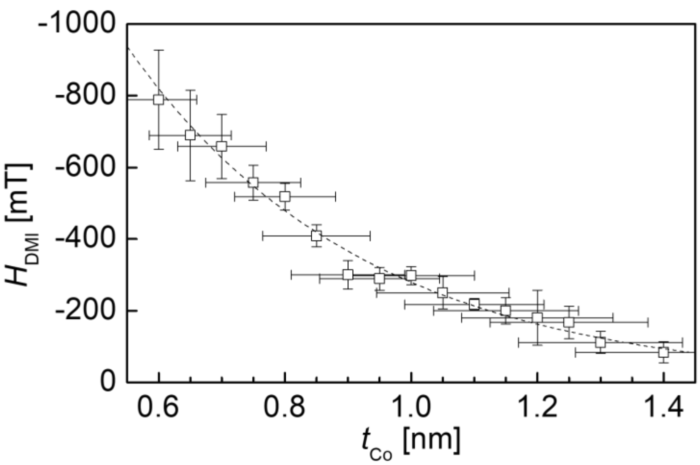

Figure 3.2 Plot of H_{DMI} with respect to t_{Co}. The dashed line guides the eyes.

Chapter 4

Non-magnetic layer thickness dependence of DMI

In this chapter, we explore the impact of non-magnetic layer thickness on the DMI in the Pt/Co single interface system. By systematically varying the Pt layer thickness, we investigate the behavior of interfacial DMI. Surprisingly, we find a significant dependence of DMI on the non-magnetic layer thickness, contrary to theoretical expectations. Moreover, X-ray diffraction (XRD) reveals an intriguing correlation between DMI and the lattice constant of Pt. This correlation is further validated by first-principles study. Furthermore, utilization of the clearly established correlation presents chirality manipulation in conventional systems.

4.1 Background

In contrast to the well-established interfacial behavior observed in the magnetic layer thickness dependence of DMI, the non-magnetic layer thickness dependence of DMI remains unclear due to the inconsistency between recent experimental results and theoretical expectations [29-34]. One potential explanation for these discrepancies could be the presence of multiple interfaces in the experimental setup, especially in magnetic layers where both top and bottom interfaces exist. As a result, mutual interactions between these interfaces might occur, as interfacial DMI is significantly influenced by various electronic properties, crystalline structures, and interface conditions. These factors introduce additional complexities that are not fully accounted for in theoretical models, leading to deviations between the predicted and observed results.

In this study, we focus on investigating the non-magnetic layer thickness dependence of DMI in Pt/Co single interface systems. By isolating and analyzing the DMI behavior without any potential mutual interference between interfaces, we can gain a clear and focused understanding of the thickness dependence of DMI.

4.2 Sample fabrication

In this study, we prepared a series of thin films with a structure of 5.0-nm Ta/t_{Pt}-nm Pt/0.8-nm Co on Si/100-nm SiO_2 substrates using dc magnetron sputtering. The deposition temperature was maintained at ~330K to optimize the magnetic signal in our system. We systematically varied the thickness of the Pt layer t_{Pt} ranging from 1.5 nm to 8.0 nm, corresponding to 7 atomic ML to 40 atomic ML. To investigate the interfacial DMI, we transferred the fabricated films to the measurement chamber through a transfer tube, employing a motorized 3-direction XYZ stage for accurate positioning. The in-vacuum DMI measurements were carried out using a MOKE microscope, which facilitated the observation and analysis of the asymmetric DW speed. A schematic of the sample structures used in this study is provided in Fig. 4.1.

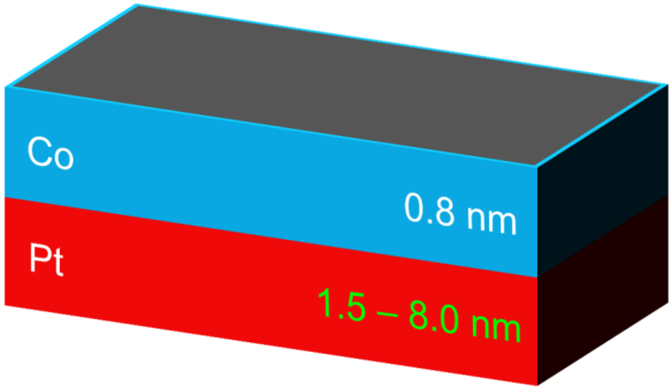

Figure 4.1 Schematic of sample structures of Pt/Co.

4.3 Non-magnetic layer thickness dependence of DMI

For each film, we conducted measurements of the asymmetric DW speed v_{DW} while sweeping an in-plane magnetic field H_x under the application of a constant out-of-plane magnetic field H_z. Figure 4.2 shows the plots of v_{DW} as a function of H_x for the Pt/Co single interface films of different t_{Pt} as indicated in each panel.

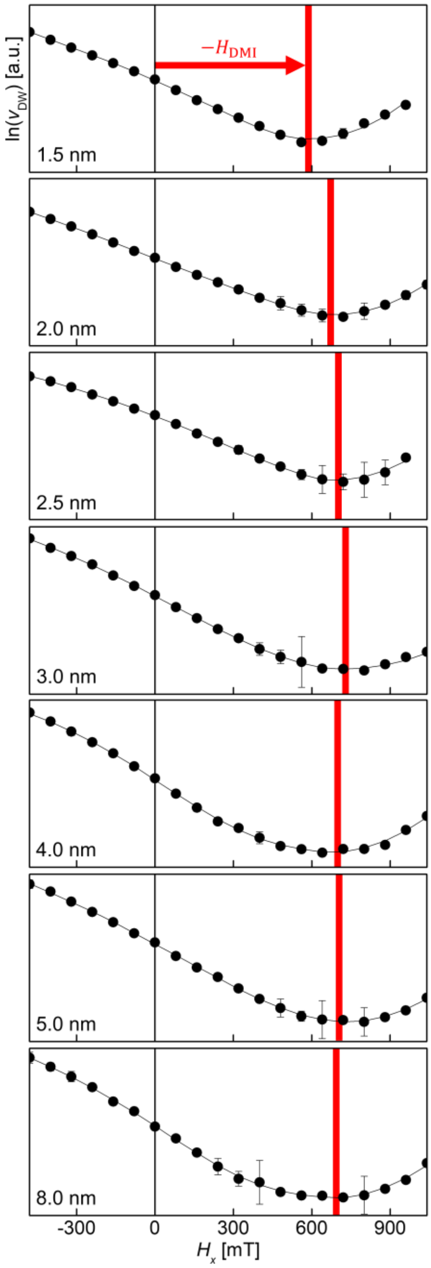

Figure 4.2 Plots of v_{DW} as a function of H_x with constant H_z for the Pt/Co single interface films with different t_{Pt}. The red vertical line indicates the symmetric axis. The value of t_{Pt} is denoted in each panel.

The figure clearly demonstrates the presence of asymmetric DW speed, where $v_{\mathrm{DW}}(H_x) \neq v_{\mathrm{DW}}(-H_x)$ for the inversion of H_x. Instead, the symmetry center is shifted to one side, as indicated by the red vertical line in each panel. According to Ref. [14], the position of the symmetry center corresponds to the value of $-H_{\mathrm{DMI}}$, where H_{DMI} is the interfacial DMI-induced effective magnetic field. Remarkably, our observations suggest that the Pt/Co interfaces exhibit a negative H_{DMI}, indicating a counterclockwise chirality of the DW configuration. This result represents the first direct experimental verification of theoretical predictions that negative interfacial DMI is generated in Pt/Co single interface [29].

Figure 4.3a shows the plot of H_{DMI} with respect to t_{Pt}. The plot demonstrates a gradual change in H_{DMI}, which eventually saturates as t_{Pt} increases. The variation in H_{DMI} is substantial, reaching up to 25% of its maximum magnitude. Notably, this H_{DMI} variation cannot be attributed to the proximity effect of additional Pt atomic layers near the interface, as the thickness of t_{Pt} exceeds 7 monoatomic layers for the thinnest t_{Pt} (= 1.5 nm). Theoretical predictions suggest that H_{DMI} variation should saturate within 2 or 3 monoatomic layers [29].

To further analyze the strength of the interfacial DMI, D, we can estimate the DW width λ using the relation $\lambda = \sqrt{A_{\mathrm{ex}}/K_{\mathrm{eff}}}$, where A_{ex} is the exchange stiffness constant and K_{eff} is effective magnetic anisotropy constant. Based on the typical value range of experimental K_{eff} ($= 1.0 \sim 1.5 \times 10^6$ J/m^3) and the literature value of A ($= 2.2 \times 10^{-11}$ J/m) of fcc Co [35-36], λ could be estimated as 4.2 ± 0.6 nm, falling within the typical range observed in various Co films. Then, with the literature value of the saturation magnetization M_S $(= 1.4 \times 10^6$ A/m$)$, D can be then estimated from the measured values of H_{DMI} through the relation $D = \lambda M_S H_{\mathrm{DMI}}$. Figure 4.3b shows the plot of the estimated value D as a function of t_{Pt}. Remarkably, D is estimated to be approximately -4.3 mJ/m^2, which is nearly close to the theoretical prediction from Pt/Co single interfaces [29]. This agreement reinforces the validity of our single interface measurement and allows for a direct comparison between experimental observations and theoretical predictions.

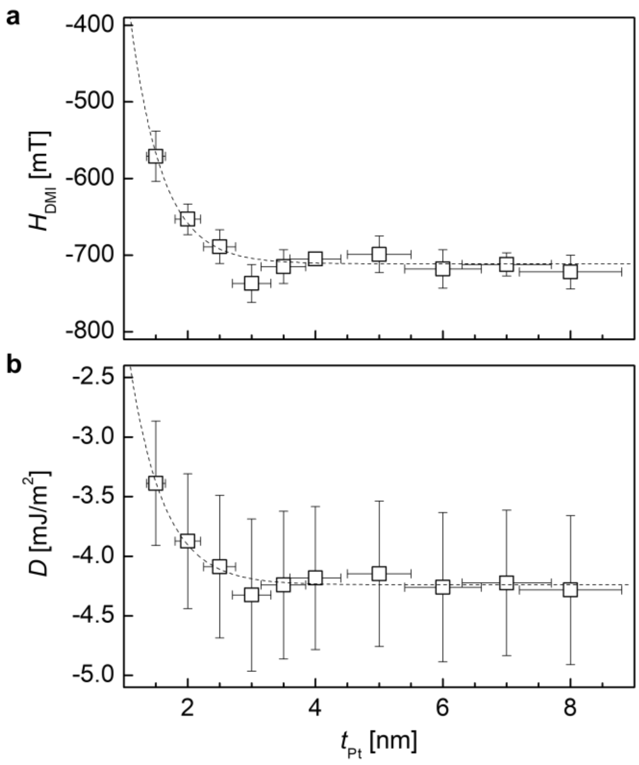

Figure 4.3 Plots of H_{DMI} and D with respect to t_{Pt}. a, Plot of H_{DMI} with respect to t_{Pt}. b, Plot of D with respect to t_{Pt}. The dashed line in each panel guides the eyes.

4.4 Correlation between DMI and lattice constant

To investigate the potential reasons behind the variation in H_{DMI}, we conducted X-ray diffraction (XRD) measurements to examine the crystalline structure of the Pt layers.

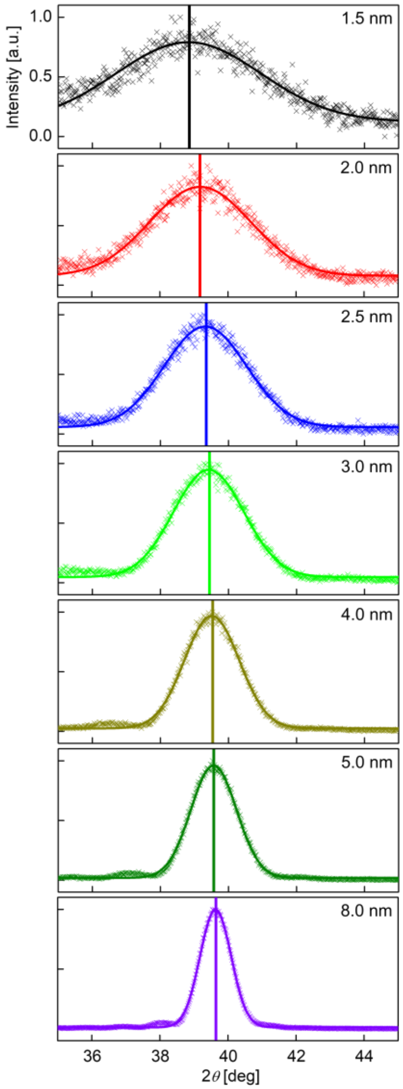

Figure 4.4 XRD spectra for the films with different t_{Pt}. The spectra near the Pt

fcc (111) peak are shown. The colored vertical line indicates the peak position. The value of t_{Pt} is denoted in each panel.

Figure 4.4 shows the XRD measurement results for the films with different t_{Pt}, as indicated in each panel. All XRD spectra exhibit a distinct peak around $2\theta \cong 39°$, which corresponds to the fcc (111) crystalline structure of the Pt layers. Upon close inspection, we observed a gradual shift of the fcc (111) peak position to one side as t_{Pt} increases. To quantify this, we converted the lattice constant c of the Pt layer from each XRD peak position. Figure 4.5a depicts the plot of c with respect to t_{Pt}.

Notably, in the thinner t_{Pt} cases, c deviates significantly from the bulk value (horizontal dashed line). However, as t_{Pt} increases, c gradually converges to the bulk value. This observation aligns with the natural growth of the film towards the bulk with increasing thickness. Figure 4.5b presents a correlation plot between c and D. Interestingly, we observed a strong correlation with a Pearson correlation coefficient $r \cong 0.95$ between c and D, indicating a possible relationship between the interfacial DMI and the lattice constant. This correlation suggests that the lattice constant of the Pt layers may play a significant role in influencing the interfacial DMI in our Pt/Co single interface systems. Furthermore, this correlation is validated by our first-principles study based on Pt/Co structure, wherein the lattice constant of Pt is varied as depicted in Fig. 4.5c.

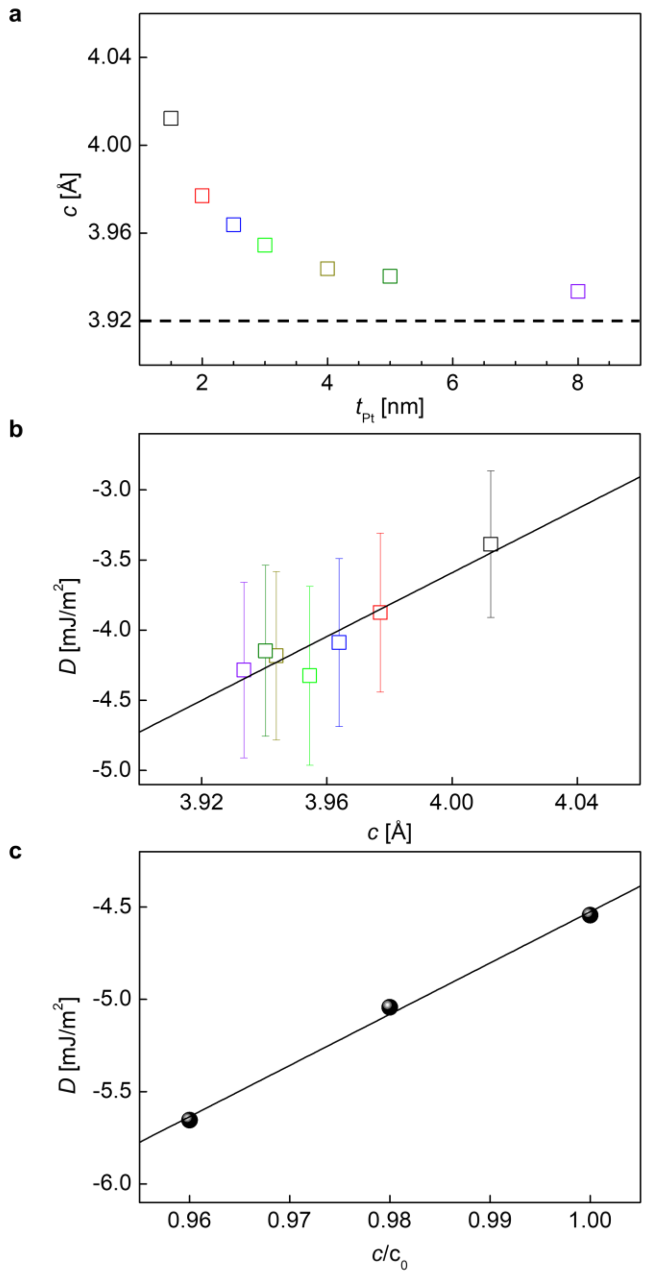

Figure 4.5 Correlation between c and D. a, Plot of c with respect to t_{Pt}. The black dashed horizontal line indicates the bulk value of the Pt fcc (111) lattice

constant. b, Plot of experimental D with respect to c. The black solid line shows the best linear fitting. c, Plot of theoretical D with respect to c/c_0 from the first-principles calculation for the Pt (1 ML)/Co (4 ML) structure. The black solid line shows the best linear fitting.

4.5 Utilization of the correlation: chirality engineering

Engineering DW chirality is a crucial technological challenge in spintronic applications involving skyrmions and chiral DWs [13-14, 21-23]. Numerous efforts have been dedicated to controlling DW chirality through materials selection or interface manipulation. Our present findings offer an alternative approach to engineer DW chirality, enabling a transition from clockwise to counterclockwise. In Fig. 4.6, we present plots of v_{DW} as a function of H_x under the application of a constant out-of-plane magnetic field H_z. Pt/Co/Pt tri-layered films with varying t_{Pt} as indicated in each panel. Notably, an additional Pt capping layer is deposited onto the Pt/Co single interface films, where the Pt capping layer thickness is fixed at 1.5 nm. Consequently, the net interfacial DMI is determined by a counterbalance between the two sources of interfacial DMIs from the bottom Pt/Co and top Co/Pt interfaces.

As depicted in Fig. 4.6, as t_{Pt} increases, H_{DMI} varies from positive to negative. The H_{DMI} variation in the Pt/Co/Pt films (Fig. 4.6) closely matches that observed in the Pt/Co films (Fig. 4.2). This observation leads to a reasonable speculation that the H_{DMI} variation is primarily influenced by the properties of the bottom Pt/Co interface, while the interfacial DMI generation at the top Co/Pt interface is less sensitive to the bottom Pt crystalline structure due to its location beyond the Co layer.

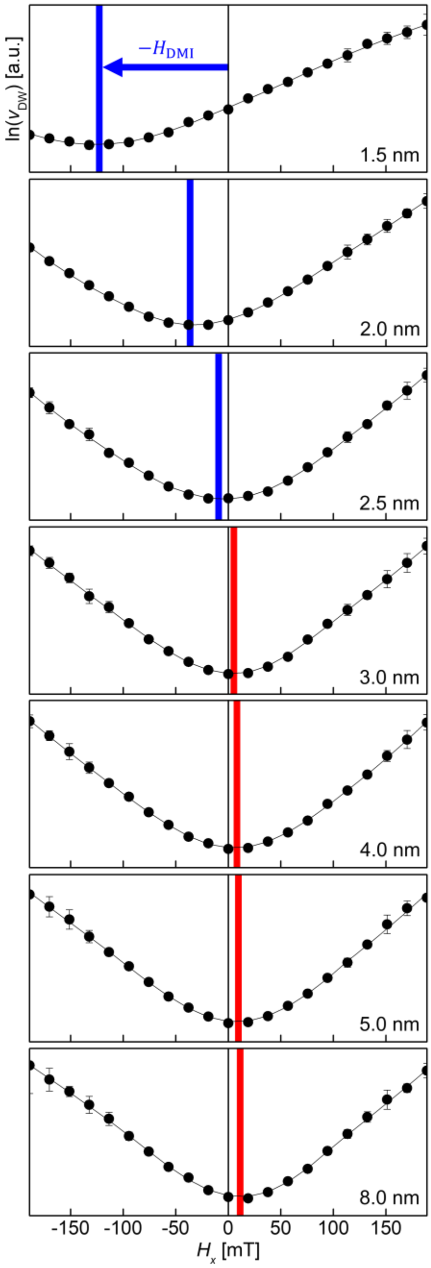

Figure 4.6 Plots of v_{DW} as a function of H_x with constant H_z for the Pt/Co/Pt

tri-layered films with different t_{Pt}. The colored vertical line indicates the symmetric axis. The value of t_{Pt} is denoted in each panel.

Due to the sign inversion of H_{DMI}, the DW chirality can be controlled, allowing for a transition from clockwise to counterclockwise configurations. This result highlights the potential for controlled chirality engineering in practical spintronic applications.

In summary, our observations showed a pronounced dependence of interfacial DMI on the non-magnetic layer thickness, contrary to theoretical expectations. Through our investigation, we identified a possible origin for this dependence, which is the lattice constant of Pt. Our first-principles study provided further support for this strong correlation. By utilizing this correlation, we achieve a systematic chirality manipulation. These results reinforce our observations in Pt/Co single interface systems.

Chapter 5

Formation of interface and DMI

In this chapter, utilizing the advanced capabilities of our in-vacuum MOKE system, we conduct a systematic investigation into the emergence of DMI for various materials. The study involves Pt/Co/X structures, where X represents different materials like Al, Cu, Nb, Pd, Hf, and Ta. By depositing these materials onto Co with sub-atomic scale layer thickness, we carry out a well-controlled exploration of DMI. Through this process, we quantify the layer-resolved contributions of DMI for each material. Additionally, our research reveals the presence of a universal interface length that plays a crucial role in the emergence of DMI.

5.1 Background

In the previous chapters, we systematically investigated DMI in the Pt/Co single interface system by varying both the magnetic layer thickness (Chapter 3) and the non-magnetic layer thickness (Chapter 4). Our findings have provided strong evidence for the interfacial nature of DMI [26-28] and reveal possible origin of unconventional dependence of DMI on non-magnetic layer thickness [29-34]. These results significantly contribute to the general understanding of interfacial DMI, driven by structural inversion asymmetry (SIA) and/or spin-orbit interaction [9, 29, 30, 37-45].

Building upon the understanding of interfacial DMI established from the investigation of single interfaces, further in-depth studies can be conducted to explore the material dependence of DMI, as well as the role of the second interface and other related factors.

5.2 Experimental approach

In this study, we present our findings on the layer-resolved contributions of interfacial DMI at Co/X interface, where X represents various materials such as Al, Cu, Nb, Pd, Hf, and Ta. Our investigation is made possible by utilizing an in-vacuum MOKE system, which enables us to quantify the interfacial DMI contributions through the analysis of asymmetric DW speed. We conduct a systematic study of the magnetic transition from the Co/vacuum surface to the Co/X interface by sequentially depositing X onto Co with sub-atomic scale thickness. Each deposition step has an average thickness of approximately 0.05 nm, corresponding to roughly a quarter of a monoatomic layer. We meticulously measure the layer-resolved contributions up to a thickness of 1 nm for X, which is approximately equivalent to five monoatomic layers.

Figure 5.1 illustrates the schematic diagram of the step-by-step deposition process of various materials denoted as X onto the Co.

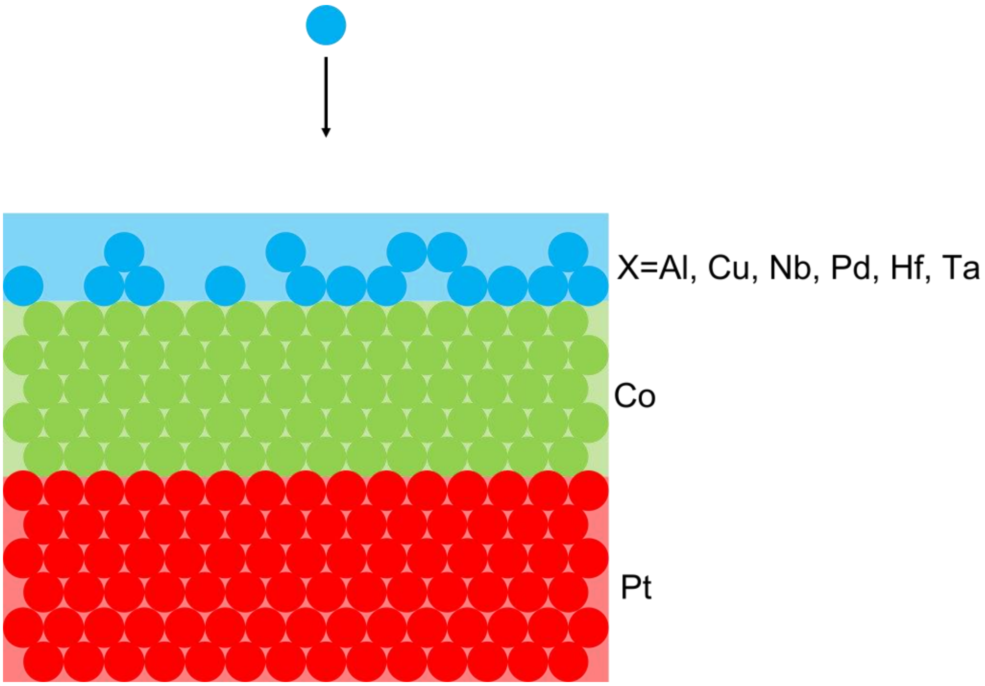

Figure 5.1 Schematic diagram of deposition process of various materials X. The used materials X is denoted in the figure.

To obtain the layer-resolved contributions of interfacial DMI at the Co/X interface, we begin the investigation by constructing a Pt/Co single interface system. Figure 5.2 illustrates the methodology used to derive the layer-resolved contributions of interfacial DMI at the Co/X interface, starting from the Pt/Co single interface system. By systematically depositing various materials denoted as X onto the Co layer, we incrementally build up the Co/X interface, allowing us to analyze the emergence of DMI at different layers and explore its material dependence.

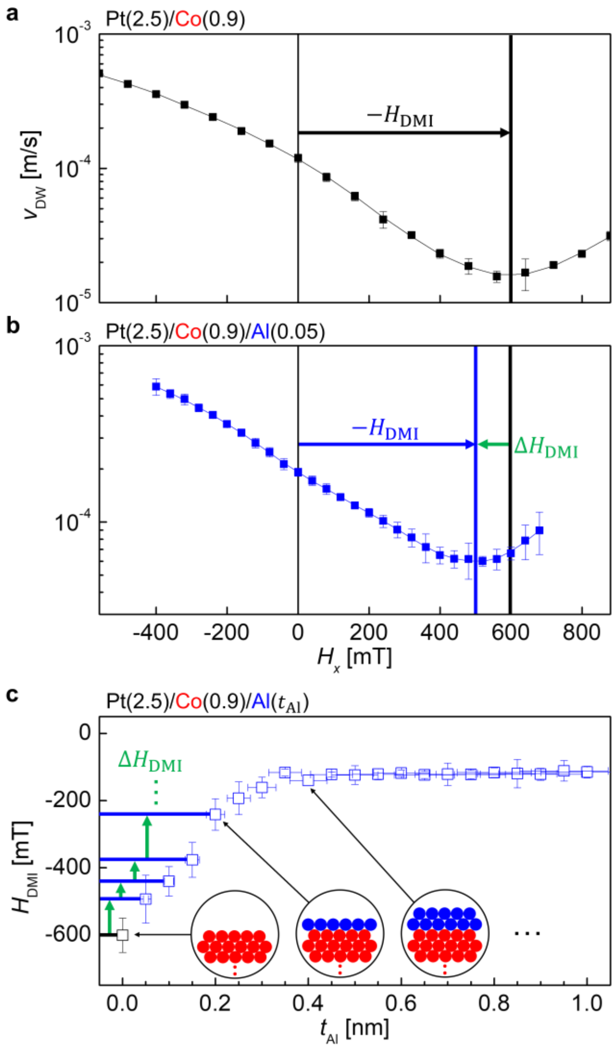

Figure 5.2 Methodology for deriving the layer-resolved contributions of interfacial DMI. a, Measurement of H_{DMI} in structure of Pt(2.5)/Co(0.9) single

interface structure. b, Measurement of H_{DMI} after first deposition of Al onto Co. The ΔH_{DMI}, difference between H_{DMI} values of Pt(2.5)/Co(0.9) and Pt(2.5)/Co(0.9)/Al(0.05) corresponds to the contribution of interfacial DMI at Co(0.9)/Al(0.05). c, Plot of H_{DMI} with respect to t_{Al} in Pt(2.5)/Co(0.9)/Al(t_{Al}). Each green vertical arrow indicates the ΔH_{DMI} for step-by-step deposition of Al. Inset shows a graphical illustration of the deposition of Al onto Co at different thicknesses, for Al(0), Al(0.2), and Al(0.4). These correspond to the Co surface, one monoatomic layer, and two monoatomic layers of Al, respectively.

By systematically depositing various materials denoted as X onto the Co layer, we incrementally build up the Co/X interface, allowing us to analyze the emergence of DMI at different layers and explore its material dependence.

5.3 Layer-resolved contributions of DMI

In this chapter, we present the results of our investigation into the layer-resolved contributions of interfacial DMI for various materials. These contributions were analyzed using the methodology discussed in the previous chapter (chapter 5.2).

X=Al

Figure 5.3 shows the plot of ${H_{\mathrm{DMI}}}^{\mathrm{Tot}}$ (Black square), and ${H_{\mathrm{DMI}}}^{\mathrm{X}}$ (Colored bar) with respect to the thickness of non-magnetic layer t_{X}, where the material X=Al. ${H_{\mathrm{DMI}}}^{\mathrm{Tot}}$ indicates the total interfacial DMI from both Pt/Co and Co/X, and ${H_{\mathrm{DMI}}}^{\mathrm{X}}$

indicates the contribution of interfacial DMI solely from Co/X, obtained from ΔH_{DMI}. In the plot, the red bar represents the contribution from the first atomic monolayer, the blue bar indicates the contributions from the second atomic monolayer, the cyan bar indicates the contributions from the third atomic monolayer, and so on. Each bar corresponds to the layer-resolved contributions of interfacial DMI originating from different atomic monolayers of the non-magnetic material (X) adjacent to the magnetic layer (Co).

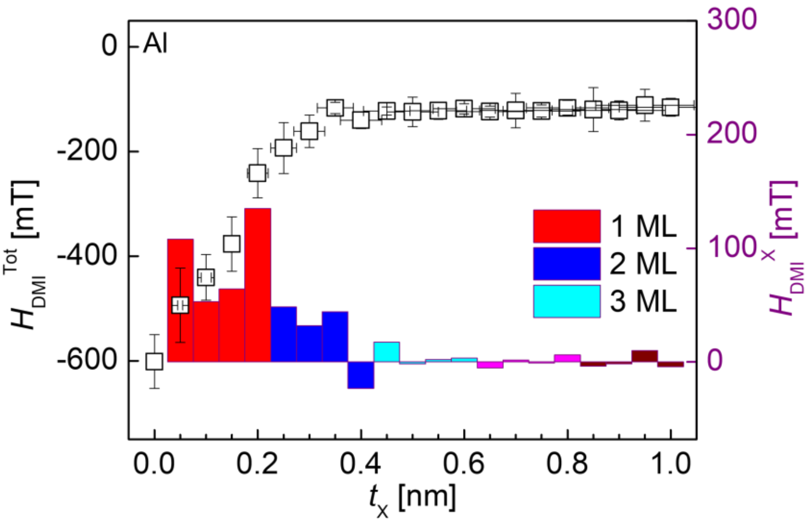

Figure 5.3 Plot of $H_{\mathrm{DMI}}{}^{\mathrm{Tot}}$ and $H_{\mathrm{DMI}}{}^{\mathrm{X}}$ with respect to t_{X} for X=Al.

Remarkably, the total interfacial DMI $H_{\mathrm{DMI}}{}^{\mathrm{Tot}}$ exhibits a smooth increase as t_{X} increases, indicating that the gradual emergence of interfacial DMI from the Co/X interface $H_{\mathrm{DMI}}{}^{\mathrm{X}}$ as t_{X} increases. As t_{X} continues to grow, $H_{\mathrm{DMI}}{}^{\mathrm{Tot}}$ eventually reaches saturation at approximately $t_{\mathrm{X}} \geq 0.4$ nm, signifying that $H_{\mathrm{DMI}}{}^{\mathrm{X}}$ converges to zero. These results strongly suggest that the interfacial DMI primarily originates from the two atomic monolayers of material X adjacent to the Co layer.

X=Cu

Continuing our analysis for other materials. Figure 5.4 shows the plot of $H_{\mathrm{DMI}}^{\mathrm{Tot}}$ (Black square), and $H_{\mathrm{DMI}}^{\mathrm{X}}$ (Colored bar) with respect to the thickness of non-magnetic layer t_{X}, where the material X=Cu.

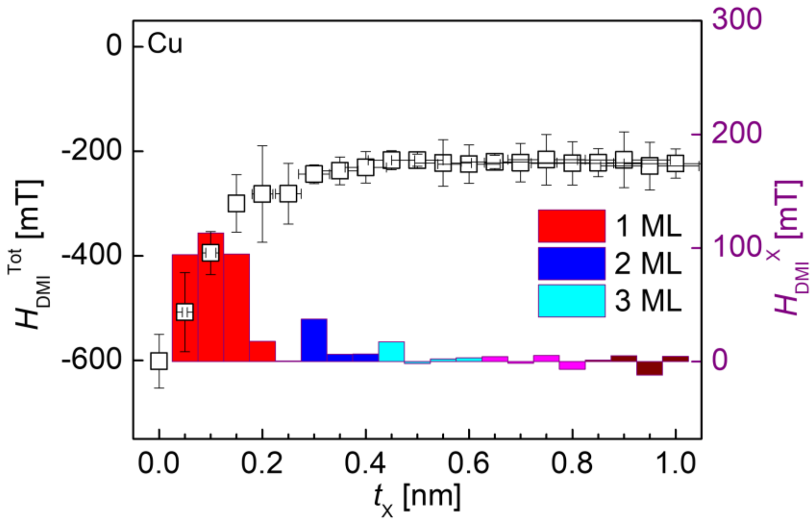

Figure 5.4 Plot of $H_{\mathrm{DMI}}^{\mathrm{Tot}}$ and $H_{\mathrm{DMI}}^{\mathrm{X}}$ with respect to t_{X} for X=Cu.

X=Nb

Continuing our analysis for other materials. Figure 5.5 shows the plot of $H_{\mathrm{DMI}}^{\mathrm{Tot}}$ (Black square), and $H_{\mathrm{DMI}}^{\mathrm{X}}$ (Colored bar) with respect to the thickness of non-magnetic layer t_{X}, where the material X=Nb.

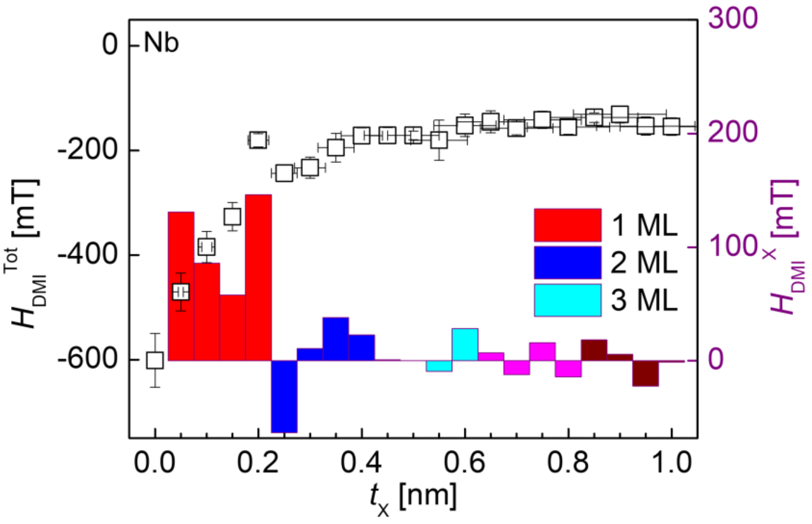

Figure 5.5 Plot of $H_{\mathrm{DMI}}{}^{\mathrm{Tot}}$ and $H_{\mathrm{DMI}}{}^{\mathrm{X}}$ with respect to t_{X} for X=Nb.

In the case of Nb, the interfacial DMI exhibits an overshoot-like emergence at approximately 0.2 nm, which is near one monoatomic layer. However, the overall behavior of its emergence occurs gradually.

X=Pd

Continuing our analysis for other materials. Figure 5.6 shows the plot of $H_{\mathrm{DMI}}{}^{\mathrm{Tot}}$ (Black square), and $H_{\mathrm{DMI}}{}^{\mathrm{X}}$ (Colored bar) with respect to the thickness of non-magnetic layer t_{X}, where the material X=Pd.

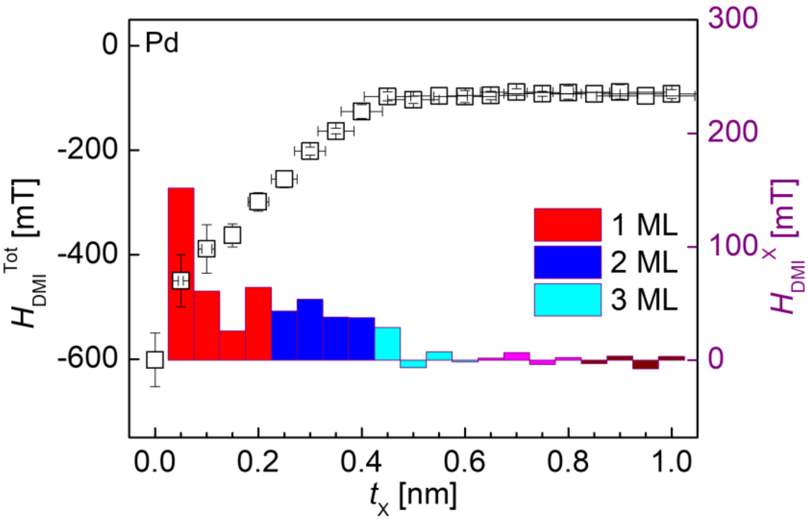

Figure 5.6 Plot of $H_{DMI}{}^{Tot}$ and $H_{DMI}{}^{X}$ with respect to t_X for X=Nb.

X=Hf

Continuing our analysis for other materials. Figure 5.7 shows the plot of $H_{DMI}{}^{Tot}$ (Black square), and $H_{DMI}{}^{X}$ (Colored bar) with respect to the thickness of non-magnetic layer t_X, where the material X=Hf.

Interestingly, careful observation of the emergence of interfacial DMI for Al, Cu, Nb, Pd, and Hf, reveals a common nature: Firstly, each atomic monolayer has positive contribution of interfacial DMI, indicating that the Co/X interface generates an interaction that prefers clockwise chirality. Secondly, while the shape of the emergence varies for each material, it occurs gradually. Thirdly, the primary contribution to the interfacial DMI originates from two atomic monolayers adjacent to Co, as initially mentioned.

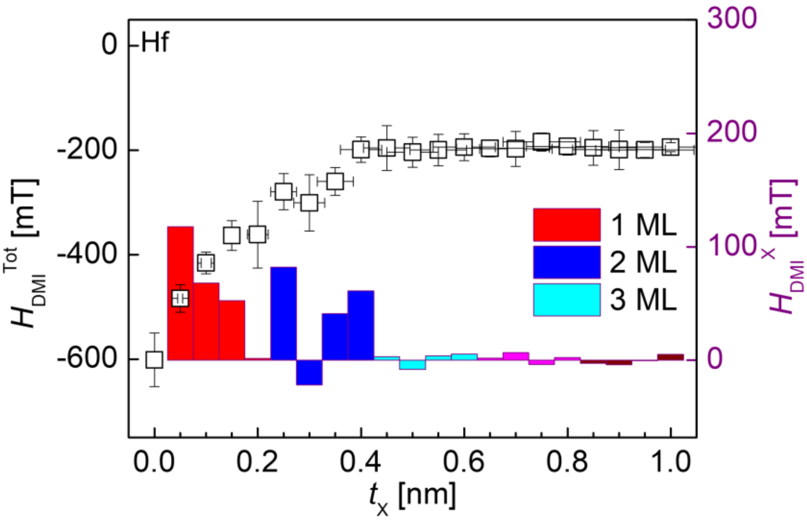

Figure 5.7 Plot of H_{DMI}^{Tot} and H_{DMI}^{X} with respect to t_X for X=Hf.

X=Ta

In the final step, we analyze the case of Ta. Figure 5.8 shows the plot of H_{DMI}^{Tot} (Black square), and H_{DMI}^{X} (Colored bar) with respect to the thickness of non-magnetic layer t_X, where the material X=Ta.

Surprisingly, there is a slight difference in the case of Ta. Although the interfacial DMI emerges gradually, it is evident that the sign of contributions for the first monolayer (positive) and the second monolayer (negative) is different. However, H_{DMI}^{Tot} begins to saturate near $t_X \geq 0.4$ nm, consistent with the behavior observed in other materials.

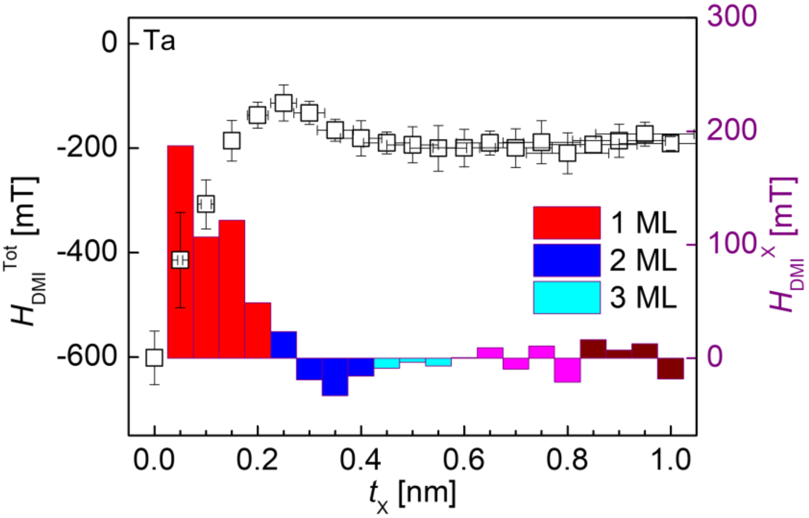

Figure 5.8 Plot of H_{DMI}^{Tot} and H_{DMI}^{X} with respect to t_X for X=Ta.

Upon closer inspection of this striking result, one can consider the coverage of deposition process. Figure 5.9 illustrates a schematic diagram of the coverage of the deposition process, showing the ideal case ($\text{Coverage} = 1$) and non-ideal case ($\text{Coverage} \neq 1$). In the ideal case, the deposition of an average thickness corresponding to 1 ML and 2 ML solely covers the atoms, generating one monoatomic layer and two monoatomic layers, respectively. However, in the non-ideal case, the deposition may not fully cover the surface, leading to incomplete layer formation.

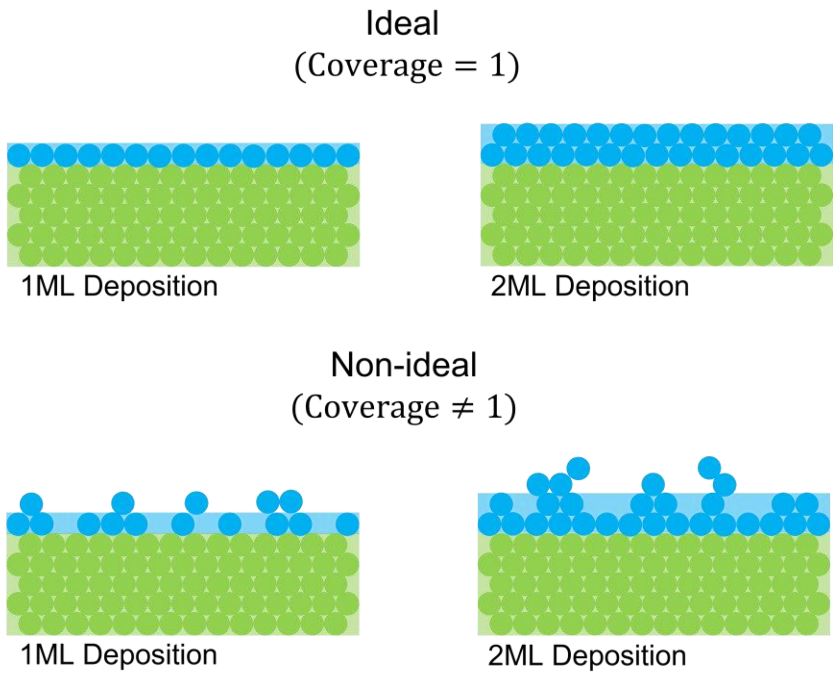

Figure 5.9 Schematic diagram of the coverage of the deposition process.

Hence, the different sign of interfacial DMI in the first atomic layer and second atomic layer of Ta may not be solely attributed to atomic coverage, as it clearly distinguishes the contribution of each layer.

To validate this observation in Ta, we conducted first-principles study on Ta based on Pt(3 ML)/Co(3 ML)/Ta(0-3 ML) structures. The result of the first-principles calculations is shown in Figure 5.10.

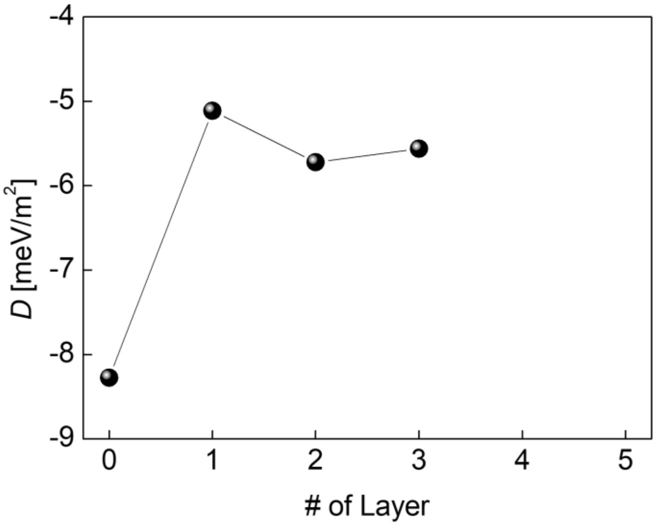

Figure 5.10 Plot of theoretical *D* with respect to number of Ta layer from the first-principles calculation for the Pt(3 ML)/Co(3 ML)/Ta(0-3 ML) structures.

Clearly, the results of the first-principles calculation indicate the different sign in the interfacial DMI contribution for the first atomic layer and the second atomic layer, consistent with the experimental observation (Fig. 5.8). Additionally, the saturation of the interfacial DMI occurs at approximately 2 ML, which is in line with the experimental observations (Fig. 5.3-5.8). To strengthen our observation further, additional calculations above Ta(3 ML) are required.

5.4 Universal length of interface: transition from surface to interface

In this chapter, we conduct an in-depth investigation of the layer-resolved contributions of interfacial DMI for various materials, which leads us to unveil the presence of a universal length of the interface that significantly influences the emergence of interfacial DMI.

To systematically study the interfacial DMI emergence during interface formation, we introduce two parameters. First, the total magnitude of interfacial DMI at the Co/X interface, denoted as ${H_{\mathrm{DMI}}}^{\mathrm{X_{Tot}}}$, represents the difference between H_{DMI} in Pt(2.5)/Co(0.9) and Pt(2.5)/Co(0.9)/X(1.0). Second, the magnitude of the accumulated interfacial DMI at the Co/X interface, denoted as $\sum {H_{\mathrm{DMI}}}^{\mathrm{X}}$, corresponds to the sum of contributions of interfacial DMI at Co/X interface up to given thickness. Specifically, $\sum {H_{\mathrm{DMI}}}^{\mathrm{X}} = {H_{\mathrm{DMI}}}^{\mathrm{X_{Tot}}}$ when the given thickness is 1.0 nm.

Afterward, we can analyze the scaled interfacial DMI emergence by calculating the ratio of theses two parameters, $\sum {H_{\mathrm{DMI}}}^{\mathrm{X}} / {H_{\mathrm{DMI}}}^{\mathrm{X_{Tot}}}$.

Figure 5.11 shows the plot of the scaled interfacial DMI emergence $\sum {H_{\mathrm{DMI}}}^{\mathrm{X}} / {H_{\mathrm{DMI}}}^{\mathrm{X_{Tot}}}$ with respect to non-magnetic layer thickness, t_{X}.

Remarkably, all the data begin to collapse near $t_{\mathrm{X}} = 0.4$ nm, reflecting our observations that the interfacial DMI primarily emerges $t_{\mathrm{X}} = 0.4$ nm, corresponding to two monoatomic layers. Consequently, we can categorize the phase of the Co/X as follows: (i) surface dominant regime, (ii) transition regime, (iii) interface dominant regime.

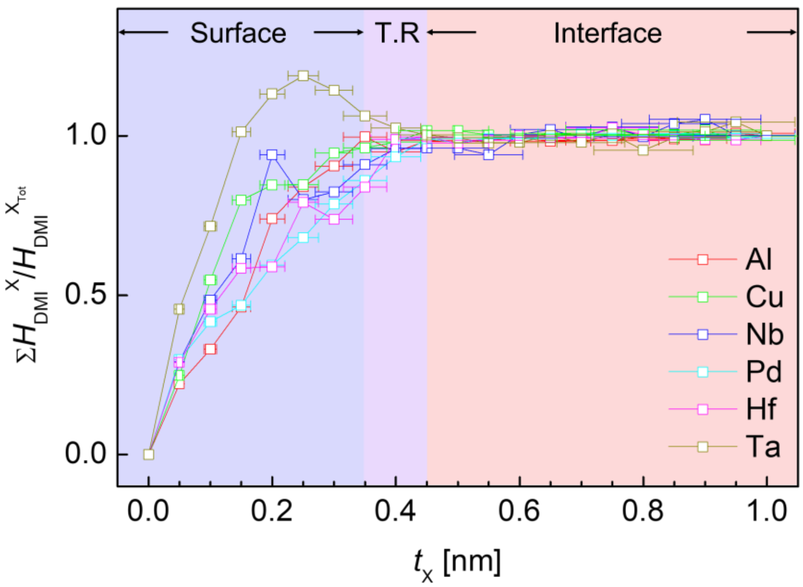

Figure 5.11 Plot of $\sum H_{\mathrm{DMI}}{}^{\mathrm{X}}/H_{\mathrm{DMI}}{}^{\mathrm{X_{Tot}}}$ with respect to t_{X}. The blue region indicates surface dominant regime. The purple region indicates transition regime from surface to interface. The red region indicates interface dominant regime.

(i) In the surface dominant regime, where $t_{\mathrm{X}} \leq 0.4$ nm, the behavior is primarily influenced by the magnetic Co surface, making it highly sensitive to even small coverage of non-magnetic materials. As a result, the interfacial DMI exhibits significant changes in this regime.

(ii) In the transition regime, where $t_{\mathrm{X}} \cong 0.4$ nm, the change in interfacial DMI initiates, but its magnitude is relatively minor compared to the surface dominant regime.

(iii) In the interface dominant regime, where $t_{\mathrm{X}} \geq 0.4\ \mathrm{nm}$, the behavior is primarily governed by the Co/X interface, and the interfacial DMI stabilizes. In this regime, the coverage of non-magnetic material becomes sufficient, and the interfacial DMI exhibits relatively minor changes compared to the two previous regimes.

In summary, our findings indicate the existence of a universal length of interface, where the behavior is primarily governed by the interface, maximizing the generation and stabilization of interfacial phenomena. Although the methodology involving magnetron sputtering may not precisely match the average thickness to the atomic layer, it still allows for well-controlled thickness control and detection of interfacial phenomena, revealing the transition from surface to interface during formation process. These findings provide not only a comprehensive understanding of the underlying nature of DMI emergence but also offer insights into the underlying mechanisms that govern this phenomenon.

Chapter 6

DW roughness scheme for DMI measurement

In this chapter, we present a novel measurement scheme specifically designed to explore DMI in weak PMA systems. Previous chapters focused on investigating DMI under relatively strong PMA conditions, where clear DW motion was observable, allowing for precise DW speed measurements to quantify interfacial DMI. However, detecting DW motion becomes challenging in weak PMA systems, making it difficult to precisely measure DMI. Therefore, we propose a new approach to quantify DMI using DW roughness measurement. This method addresses the challenges faced in DMI measurement based on DW motion in weak PMA systems.

6.1 Background

In this thesis, we focus on studying interfacial DMI using the asymmetric DW speed scheme (chapter 1.6). This method is well-suited for systems with clear DW motion, typically observed under strong PMA conditions. However, when dealing with systems exhibiting non-clear DW motion, particularly under weak PMA conditions, the situation becomes different. In such cases, DWs tend to be rougher compared to strong PMA systems [12].

Furthermore, studying dynamics can introduce potential artifacts, such as time-dependent phenomena and chiral damping [46-48]. To avoid these possible artifacts, we aim to develop a DMI measurement scheme based on static equilibrium states without any motion.

In this study, we report that it is possible to determine the strength of DMI by analyzing the static (or quasi-static) roughness of chiral DWs. This DW roughness can be measured from a single snapshot of the DW image at rest without any additional motion. By examining magnetic multilayer films of Pt/Co/Pt heterostructures, we have discovered that the DW roughness can be analyzed based on the competition between DMI and DW energies, providing insights into the quantitative determination of both magnitude and sign of the DMI-induced effective magnetic field, H_{DMI}.

6.2 Sample fabrication

The detailed stacking structure of the Pt/Co/Pt films is 5.0-nm Ta/1.75-nm Pt/0.3-

nm Co/1.5-nm Pt. The films were deposited on Si/100-nm SiO2 substrates by means of dc magnetron sputtering process. The lowermost Ta layers are buffer layers for better crystallinity of films and the topmost Pt layers are the capping layer to prevent possible oxidation and contamination.

6.3 Determination of DW roughness

To ensure better statistical analysis of the DW roughness [49-50], all DWs were created under an identical procedure by use of a gold wire patterned on the films. The gold wire (yellow area) was positioned across the magnetic wire (light gray area), as depicted in Fig. 6.1a.

Each DW writing procedure followed a specific sequence: first, the magnetization was saturated by applying an external out-of-plane magnetic field pulse. Next, an electric current pulse (blue arrow) was injected through the gold wire, generating the Oersted field (curved green arrow), as depicted in Fig. 6.1b. This switching of the magnetization in the region adjacent to the gold wire resulted in the creation of a linear DW parallel to the writing line for each DW writing procedure.

To ensure reproducibility and reliability in repeated measurements, an automatic procedure was employed to create identical DWs consistently. After every measurement, all the DW structures were completely erased by saturating the magnetization to secure the identical state for the next measurement. Figure 6.1c shows a snapshot of MOKE image of the film. The figure clearly shows a 300-μm-long straight DW along the y axis, created by an electric current pulse of 20 mA and 100 ms.

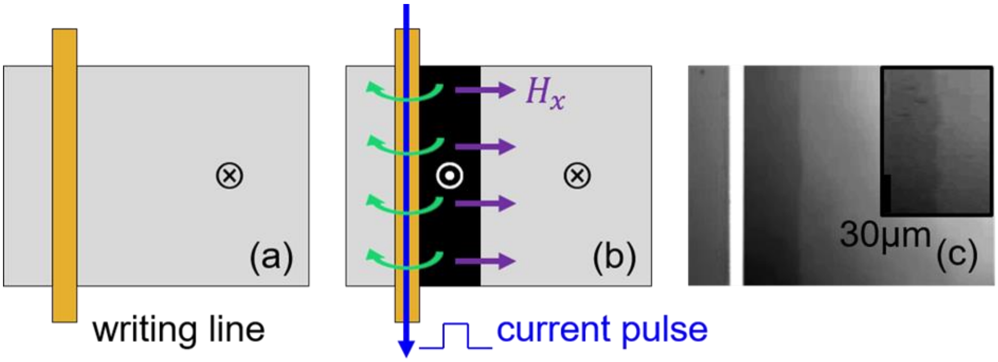

Figure 6.1 Schematic drawing of DW writing process. a, Schematic drawing of the sample with the magnetic wire (light gray area) and gold wire (yellow area). b, The reversed magnetic domain (dark gray area) by the Oersted field (curved green arrow) from the injected current pulse (blue arrow) under an external in-plane magnetic field H_x (purple arrow). c, MOKE image of the Pt/Co/Pt film at the state described in b. The inset shows the magnified image of the DW.

Looking close to the DWs, each DW exhibits local roughness as shown by the inset of Fig. 6.1c, though the DW is straight in a large scale. Such DW roughness comes from the local irregularities with quenched disorders such as defects and DW pinning sites. In the quenched disorder systems, the interfaces can be analyzed within the context of scaling laws [11, 51-52].

For quantitative analyses, the DW roughness is parameterized as the average width of the DW position fluctuation. For the present case of DWs along the y axis, the average width w is defined as the standard deviation of the DW positions in the x direction. Then, w follows the scaling law with respect to the DW segment length L as given by $w \propto (L/L_{\mathrm{C}})^{\zeta}$ for $L > L_{\mathrm{C}}$ [11]. Here, ζ $(= 2/3)$ is the roughening exponent and L_{C} is the Larkin length [11,53-55]. According to Ref. [11], L_{C} scales with the DW energy density σ_{DW} as given by $L_{\mathrm{C}} \propto \sigma_{\mathrm{DW}}^{2/3}$. Summing up these scaling relations, one can find that w follows a scaling law with respect to σ_{DW} as given by

$$w \propto \sigma_{\mathrm{DW}}^{-\eta}, \tag{6.1}$$

with $\eta = 4/9$.

It is possible to change σ_{DW} by applying an in-plane magnetic field H_x in the x direction.

For this case, σ_{DW} follows the relation $\sigma_{\mathrm{DW}}(H_x) = \sigma_0 - 2\lambda K_{\mathrm{D}} H_{\mathrm{S}}^{-2}(H_x + H_{\mathrm{DMI}})^2$ for $|H_x + H_{\mathrm{DMI}}| < H_{\mathrm{S}}$ [14-15], where σ_0 is the DW energy density at the Bloch chirality, λ is the DW width, K_{D} is the DW anisotropy, and H_{S} is the saturation field to the Néel chirality.

The $\sigma_{\mathrm{DW}}(H_x)$ variation corresponds to the DW chirality transition from a Néel chirality ($H_x < -H_{\mathrm{DMI}}$) through the Bloch chirality ($H_x = -H_{\mathrm{DMI}}$) to the other Néel chirality ($H_x > -H_{\mathrm{DMI}}$). It is worthwhile to note that the plot of $\sigma_{\mathrm{DW}}(H_x)$ shows a symmetric parabola centered at $H_x = -H_{\mathrm{DMI}}$ of the Bloch chirality. Therefore, it is possible to quantify H_{DMI} from the center of symmetry in the DW chirality transition. Since $w(H_x)$ shares the center of symmetry identical to $\sigma_{\mathrm{DW}}(H_x)$ due to the scaling relation of Eq. (6.1), the center of symmetry in $\sigma_{\mathrm{DW}}(H_x)$ can be acquired by measuring $w(H_x)$ with respect to H_x. Therefore, the experimental measurement of $w(H_x)$ provides a way to quantify H_{DMI} from the center of symmetry.

To examine whether it is possible to resolve the center of symmetry from the $w(H_x)$ measurement, we carried out the DW roughness measurement under the application of H_x. Figures 6.2a and b show the MOKE images of the linear DWs in the film, created under the application of different H_x, (a) 0 and (b) 182 mT, respectively. Interestingly, the degree of the DW roughness changes a lot with respect to H_x. The degree of the DW roughness is distinguishable even to eyes between the images. The latter DW looks noticeably rougher than the former.

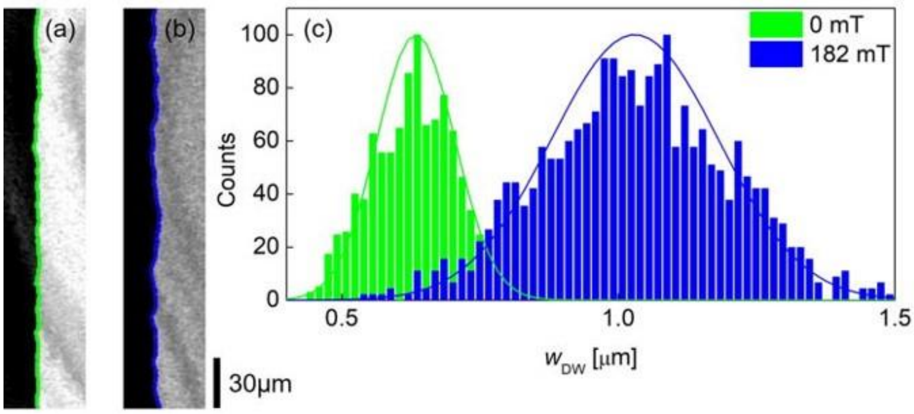

Figure 6.2 Determination of DW roughness. a, MOKE images for $H_x = 0$. b, MOKE images for $H_x = 182$ mT. c, The histogram of w for $H_x = 0$ (green) and $H_x = 182$ mT (blue), respectively.

For a quantitative comparison, $w(H_x)$ was determined from the images. For better statistical analysis, the measurement was done repeatedly by 1,000 times for each given H_x. Figure 6.2c shows the histogram of the measured 1,000 values of w

for $H_x = 0$ (green) and 182 mT (blue), respectively. Each histogram exhibits a Gaussian-like distribution for a given H_x. Therefore, we quantified the mean value $\bar{w}$ and the half width at half maximum for each Gaussian-like distribution. The distinct DW roughness in Figs. 6.2a and b corresponds to the almost twice variation of $\bar{w}$ from 0.63 μm for a to 1.03 μm for b. It is worthwhile to note that the difference in $\bar{w}$ is certainly larger than σ. Therefore, it is possible to resolve each distribution from the other.

6.4 Quantification of DMI from DW roughness

From the repeated measurements by sweeping H_x, the chirality transition of $\bar{w}$ was examined. Figure 6.3a shows the plot of $\bar{w}$ with respect to H_x. Here, the error bar corresponds to the half width at half maximum.

The clear symmetry manifests that the DW roughness is mainly governed by the DW energy density in this controlled experiment. Therefore, it is possible to quantify H_{DMI} from the DW roughness measurement. The center of symmetry in Fig. 6.3a corresponds to $H_{\mathrm{DMI}} = 78 \pm 10$ mT.

To verify the validity of the present measurement scheme, we adopted another H_{DMI} measurement scheme based on the asymmetric DW speed [14]. This scheme analyzes the DW speed v_{DW} with respect to H_x. Due to the dependence on σ_{DW}, $v_{\mathrm{DW}}(H_x)$ exhibits the chirality transition identical to $\sigma_{\mathrm{DW}}(H_x)$. Therefore, $v_{\mathrm{DW}}(H_x)$ shares the center of symmetry identical to $\sigma_{\mathrm{DW}}(H_x)$ and consequently, identical to $\bar{w}(H_x)$. Figure 6.3b plots $v_{\mathrm{DW}}(H_x)$. The figure manifests that $v_{\mathrm{DW}}(H_x)$

exhibits the center of symmetry identical to $\bar{w}(H_x)$. The exact accordance confirms the validity of both the H_{DMI} measurement schemes.

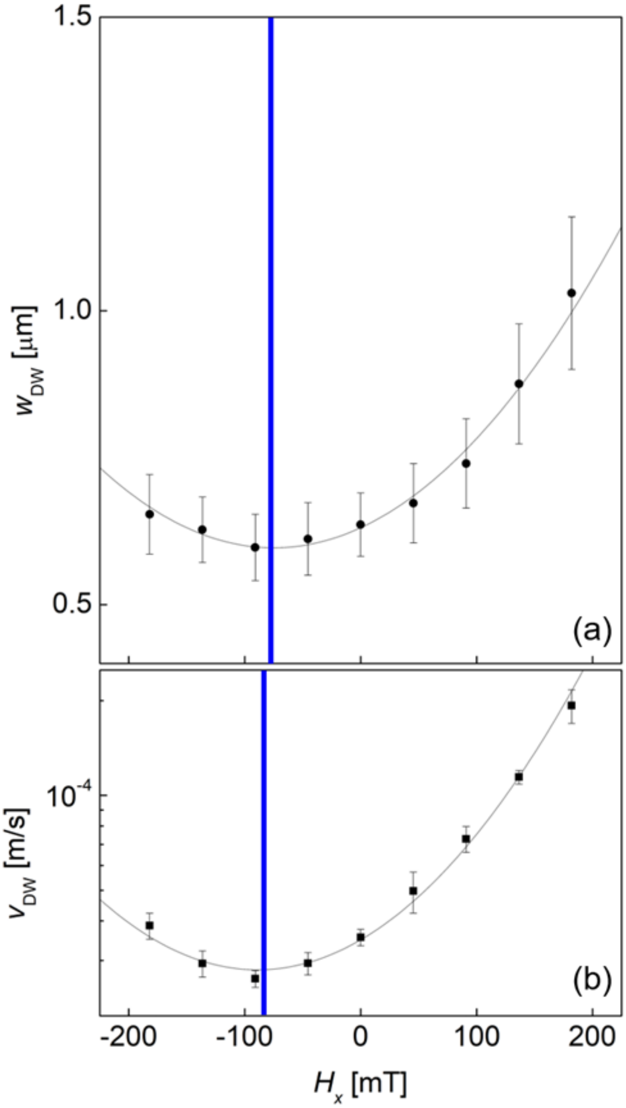

Figure 6.3 Quantification of DMI based on DW roughness and DW asymmetric speed for the Pt/Co/Pt film. a, Plot of $\bar{w}(H_x)$ with respect to H_x. b, Plot of $v_{\mathrm{DW}}(H_x)$ with respect to H_x. The vertical blue lines indicate the center of

symmetry for each panel.

In conclusion, we demonstrated that the DW roughness exhibits a symmetric variation in accordance with the DW chirality with respect to the in-plane magnetic field. The DW roughness variation was found to be large enough to resolve the center of symmetry. Since the center of symmetry corresponds to the DMI-induced effective magnetic field, the present observation enables an experimental DMI measurement scheme based on the DW roughness. The validity of the present measurement scheme was confirmed in comparison with the other measurement scheme. This new scheme provides a reliable substitute under circumstances where conventional methods may not be applicable.

Chapter 7

Conclusion and outlook

In this thesis, our research focuses on interfacial Dzyaloshinskii-Moriya interaction (DMI) at single interfaces. We investigate magnetic domain walls (DWs) in films with perpendicular magnetic anisotropy (PMA), specifically based on the Pt/Co single interface film. The primary objective is to gain a deep understanding of the Pt/Co single interface by varying the thicknesses of both the non-magnetic layer (Pt) and the magnetic layer (Co).

Through these investigations, we confirm the interfacial nature of DMI and observe an unconventional dependence of DMI on the thickness of the non-magnetic layer. To shed light on the origin of this dependency, we conduct X-ray diffraction (XRD) examinations and discover a strong correlation between DMI and the lattice constant of Pt. This correlation is further validated by our first-principles study. The clear correlation allows us to manipulate the chirality systematically in conventional magnetic systems, such as Pt/Co/Pt, from clockwise (CW) to counterclockwise (CCW) chirality. These results provide a clearer understanding of the Pt/Co single interface.

Building on the enhanced understanding of the Pt/Co single interface, we extend our research to study interfacial DMI at the Co/X interface, where X represents various materials. In this study, we quantitatively determine the layer-resolved contributions of interfacial DMI at the Co/X interface and unveil the existence of a universal length of interface, approximately two monoatomic layers, which plays a pivotal role in the emergence of interfacial DMI. Based on this universal length, we categorize the phase of the Co/X interface into three regimes: surface regime, transition regime, and interface regime, using DMI as a critical criterion. These findings provide insights into the interfacial characteristics of DMI and offer a systematic way to understand the nature of interface.

This thesis centers on a specific interfacial phenomenon called DMI. To study DMI at the single interface level, we developed an in-vacuum Magneto-Optical Kerr Effect (MOKE) system. This pioneering experimental approach allows us to gain a deeper understanding of the physics involved in interfacial phenomena compared to conventional methods. Additionally, our experimental approach serves as a problem-solving strategy that can be applied to investigate and unravel other interfacial phenomena.

References

[1] I. Dzyaloshinsky, A thermodynamic theory of weak ferromagnetism of antiferromagnetics, J. Phys. Chem. Solid. **4**, 241-255 (1958).

[2] T. Moriya, Anisotropic superexchange interaction and weak ferromagnetism, Phys. Rev. **120**, 91-98 (1960).

[3] A. Fert, and P. M. Levy, Role of anisotropic exchange interaction in determining the properties of spin-glasses, Phys. Rev. Lett. **44**, 1538-1541 (1980).

[4] K.-W. Kim, H.-W. Lee, K.-J. Lee, and M.D. Stiles, Chirality from interfacial spin-orbit coupling effects in magnetic bilayers, Phys. Rev. Lett. **111**, 216601 (2013).

[5] T. Kikuchi, T. Koretsune, R. Arita, and G. Tatara, Dzyaloshinskii-Moriya interaction as a consequence of a Doppler shift due to spin-orbit-induced intrinsic spin current, Phys. Rev. Lett. **116**, 247201 (2016).

[6] F. Freimuth, S. Blügel, and Y. Mokrousov, Berry phase theory of Dzyaloshinskii-Moriya interaction and spin-orbit torques, J. Phys. Condens. Matter. **26**, 104202 (2014).

[7] S. Kim, K. Ueda, G. Go, P.-H. Jang, K.-J Lee, A. Belabbes, A. Manchon, M. Suzuki, Y. Kotani, T. Nakamura, K. Nakamura, T. Koyama, D. Chiba, K. T. Yamada, D.-H. Kim, T. Moriyama, K.-J. Kim, and T. Ono, Correlation of the

Dzyaloshinskii-Moriya interaction with Heisenberg exchange and orbital asphericity, Nat. Commun. **9**, 1648 (2018).

[8] A. Belabbes, G. Bihlmayer, S. Blügel, and A. Manchon, Oxygen-enabled control of Dzyaloshinskii-Moriya interaction in ultra-thin magnetic films, Sci. Rep. **6**, 24634 (2016).

[9] H. Jia, B. Zimmermann, G. Michalicek, G. Bihlmayer, and S. Blügel, Electric dipole moment as descriptor for interfacial Dzyaloshinskii-Moriya interaction, Phys. Rev. Mater. **4**, 024405 (2020).

[10] P. J. Metaxas, J. P. Jamet, A. Mougin, M. Cormier, J. Ferré, V. Baltz, B. Rodmacq, B. Dieny, and R. L. Stamps, Creep and flow regimes of magnetic domain-wall motion in ultrathin Pt/Co/Pt films with perpendicular anisotropy, Phys. Rev. Lett. **99**, 217208 (2007).

[11] S. Lemerle, J. Ferré, C. Chappert, V. Mathet, T. Giamarchi, and P. L. Doussal, Doamin wall creep in an Ising ultrathin magnetic film, Phys. Rev. Lett. **80**, 849 (1998).

[12] D.-Y. Kim, M.-H. Park, Y.-K. Park, J.-S. Yu, J.-S. Kim, D.-H. Kim, B.-C. Min, and S.-B. Choe, Huge domain-wall speed variation with respect to ferromagnetic layer thickness in ferromagnetic Pt/Co/TiO_2/Pt films, Appl. Phys. Lett. **112**, 062406 (2018).

[13] D.-Y. Kim, D.-H. Kim, J. Moon, and S.-B. Choe, Determination of magnetic domain-wall types using Dzyaloshinskii-Moriya-interaction-induced domain

patterns, Appl. Phys. Lett. **106**, 262403 (2015).

[14] S.-G. Je, D.-H. Kim, S.-C. Yoo, B.-C. Min, K.-J. Lee, and S.-B. Choe, Asymmetric magnetic domain-wall motion by the Dzyaloshinskii-Moriya interaction, Phys. Rev. B. **88**, 214401 (2013).

[15] S.-G. Je, S.-C. Yoo, J.-S. Kim, Y.-K. Park, M.-H. Park, J. Moon, B.-C. Min, and S.-B. Choe, Emergence of huge negative spin-transfer torque in atomically thin Co layers, Phys. Rev. Lett. **118**, 167205 (2017).

[16] P. F. Carcia, A. D. Meinhaldt, and A. Suna, Perpendicular magnetic anisotropy in Pd/Co thin film layered structures, Appl. Phys. Lett. **47**, 178-180 (1985).

[17] G. Bihlmayer, Y. M. Koroteev, P. M. Echenique, E. V. Chulkov, and S. Blügel, The Rashba-effect at metallic surfaces, Surface science, **600**(18), 3888-3891 (2006).

[18] L. W. Molenkamp, G. Schmidit, and G. E. W. Bauer, Rashba Hamiltonian and electron transport, Phys. Rev. B. **64**, 121202® (2001).

[19] J. Sinova, S. O. Valenzuela, J. Wuderlich, C. H. Back, and T. Jungwirth, Spin Hall effects, Rev. Mod. Phys. **87**, 1213 (2015).

[20] J. E. Hirsch, Spin Hall effect, Phys. Rev. Lett. **83**, 1834 (1999).

[21] S. S. P. Parkin, M. Hayashi, and L. Thomas, Magnetic domain-wall racetrack memory, Science, **320**(5873) 190-194 (2008).

[22] S. Parkin, and S.-H. Yang, Memory on the racetrack, Nat. Nanotechnol. 10(3),

195-198 (2015).

[23] K.-W. Moon, D.-H. Kim, S.-C. Yoo, S.-G. Je, B. S. Chun, W. Kim, B.-C. Min, C. Hwang, and S.-B. Choe, Magnetic bubblecade memory based on chiral domain walls, Sci. Rep. **5**(1), 9166 (2015).

[24] A. Fert, V. Cros, and J. Sampaio, Skyrmions on the track, Nat. Nanotechnol. **8**, 152-156 (2013).

[25] W. Jiang, P. Upadhyaya, W. Zhang, G. Yu, M. B. Jungfleisch, F. Y. Fradin, J. E. Pearson, Y. Tserkovnyak, K. L. Wang, O. Heinonen, S. G. E. T. Velthuis, and A. Hoffmann, Blowing magnetic skyrmion bubbles, Science, **349**(6245) 283-286 (2015).

[26] J. Cho, N.-H. Kim, S. Lee, J.-S. Kim, R. Lavrijsen, A. Solignac, Y. Yin, D.-S. Han, N. J. J. van Hoof, H. J. M. Swagten, B. Koopmans, and C.-Y. You, Thickness dependence of the interfacial Dzyaloshinskii-Moriya interaction in inversion symmetry broken systems, Nat. Commun. **6**, 7635 (2015).

[27] Y.-K. Park, J.-S. Kim, Y.-S. Nam, S. Jeon, J.-H. Park, K.-W. Kim, H.-W. Lee, B.-C. Min, and S.-B. Choe, Interfacial atomic layers for full emergence of interfacial Dzyaloshinskii-Moriya interaction, NPG. A. Mater. **12**, 38 (2020).

[28] H. T. Nembach, J. M. Shaw, M. Weiler, E. Jué, and T. J. Silva, Linear relation between Heisenberg exchange and interfacial Dzyaloshinskii-Moriya interaction in metal films, Nat. Phys. **11**, 825-829 (2015).

[29] H. Yang, A. Thiaville, S. Rohart, A. Fert, and M. Chshiev, Anatomy of

Dzyaloshinskii-Moriya interaction at Co / Pt interfaces, Phys. Rev. Lett. **115**, 267210 (2017).

[30] H. Jia, B. Zimmermann, and S. Blügel, First-principles investigation of chiral magnetic properties in multilayers: Rh/Co/Pt and Pd/Co/Pt, Phys. Rev. B. **98**, 144427 (2018).

[31] N.-H. Kim, D.-S. Han, J. Jung, K. Park, H. J. M. Swagten, J.-S. Kim, and C.-Y. You, Dependence of interfacial Dzyaloshinskii-Moriya interaction and perpendicular magnetic anisotropy on the thickness of the heavy-metal layer, Appl. Phys. Express. **10**, 103003 (2017).

[32] S. Tacchi, R. E. Troncoso, M. Ahlberg, G. Gubbiotti, M. Madami, J. Åkerman, and P. Landeros, Interfacial Dzyaloshinskii-Moriya interaction in Pt / CoFeB films:effect of the heavy-metal thickness, Phys. Rev. Lett. **118**, 147201 (2017).

[33] H. Yang, O. Boulle, V. Cros, A. Fert, and M. Chshiev, Controlling Dzyaloshinskii-Moriya interaction via chirality dependent atomic-layer stacking, insulator capping and electric field, Sci. Rep. **8**, 12356 (2018).

[34] W. Legrand, Y. Sassi, F. Ajejas, S. Collin, L. Bocher, H. Jia, M. Hoffmann, B. Zimmermann, S. Blügel, N. Reyren, V. Cros, and A. Thiaville, Spatial extent of the Dzyaloshinskii-Moriya interaction at metallic interfaces, Phys. Rev. Mater. **6**, 024408 (2022).

[35] P. J. Metaxas, J. P. Jamet, A. Mougin, M. Cormier, J. Ferré, V. Baltz, B. Rodmacq, B. Dieny, and R. L. Stamps, Creep and flow regimes of magnetic domain-wall

motion in ultrathin Pt / Co / Pt films with perpendicular anisotropy, Phys. Rev. Lett. **99**, 217208 (2007).

[36] D.-Y. Kim, N.-H. Kim, Y.-K. Park, M.-H. Park, J.-S. Kim, Y.-S. Nam, J. Jung, J. Cho, D.-H. Kim, J.-S. Kim, B.-C. Min, S.-B. Choe, and C.-Y. You, Quantitative accordance of Dzyaloshinskii-Moriya interaction between domain-wall and spin-wave dynamics, Phys. Rev. B. **100**, 224419 (2019).

[37] S. Mankovsky, S. Polesya, and H. Ebert, Spin-wave stiffness and micromagnetic exchange interactions expressed by means of the KKR Green function approach, Phys. Rev. B. 99, 104427 (2019).

[38] F. Mahfouzi, and N. Kioussis, First-principles calculation of the Dzyaloshinskii-Moriya interaction: a Green's function approach, Phys. Rev. B. **103**, 094410 (2021).

[39] L. Bergqvist, A. Taroni, A. Bergman, C. Etz, and O. Eriksson, Atomistic spin dynamics of low-dimensional magnets, Phys. Rev. B. **87**, 144401 (2013).

[40] L. Rózsa, L. Udvardi, L. Szunyogh, and I. A. Szabó, Magnetic phase diagram of an Fe monolayer on W(110) and Ta(11) surfaces based on *ab initio* calculations, Phys. Rev. B. **91**, 144424 (2015).

[41] G. J. Vida, E. Simon, L. Rózsa, K. Palotás, and L. Szunyogh, Domain-wall profiles in Co/Ir_n/Pt(111) ultrathin films: influence of the Dzyaloshinskii-Moriya interaction, Phys. Rev. B. **94**, 214422 (2016).

[42] E. Simon, L. Rózsa, K. Palotás, and L. Szunyogh, Magnetism of a Co monolayer

on Pt (111) capped by overlayers of 5*d* elements: a spin-model study, Phys. Rev. B. **97**, 134405 (2018).

[43] B. Zimmermann, G. Bihlmayer, M. Böttcher, M. Bouhassoune, S. Lounis, J. Sinova, S. Heinze, S. Blügel, and B. Dupé, Comparison of first-principles method to extract magnetic parameters in ultrathin films: Co/Pt(111), Phys. Rev. B. **99**, 214426 (2019).

[44] B. Nagyafalusi, L. Udvardi, L. Szunyogh, and L. Rózsa, Spin reorientation transition in an ultrathin Fe film on W(110) induced by Dzyaloshinsky-Moriya interactions, Phys. Rev. B. **102**, 134413 (2020).

[45] P. C. Carvalho, I. P. Miranda, A. B. Klautau, A. Bergman, and H. M. Petrilli, Complex magnetic textures in Ni/Ir_n/Pt(111) ultrathin films, Phys. Rev. Mater. **5**, 124406 (2021).

[46] E. Jué, C. K. Safeer, M. Drouard, A. Lopez, P. Balint, L. Buda-Prejbeanu, O. Boulle, S. Auffret, A. Schuhl, A. Manchon, I. M. Miron, and G. Gaudin, Chiral damping of magnetic domain walls, Nat. Mater. **15**, 272-277 (2016).

[47] K.-W. Kim, and H.-W. Lee, Chiral damping, Nat. Mater. **15**, 253-254 (2016).

[48] A. V. Davydenko, A. G. Kozlov, M. E. Stebliy, A. G. Kolesnikov, N. I. Sarnavskiy, I. G. Iliushin, and A. P. Golikov, Dzyaloshinskii-Moriya interaction and chiral damping effect in symmetric epitaxial Pd/Co/Pd(111) trilayers, Phys. Rev. B. **103**, 094435 (2021).

[49] D. Jordán, L. J. Albornoz, J. Gorchon, C. H. Lambert, S. Salahuddin, J. Bokor, J.

Curiale, and S. Bustingorry, Statistically meaningful measure of domain-wall roughness in magnetic thin films, Phys. Rev. B. 101, 184431 (2020)

[50] Y. Zhang, X. Zhang, N. Vernier, Z. Zhang, G. Agnus, J. Coudevylle, X. Lin, Y. Zhang, Y. Zhang, W. Zhao, and D. Ravelosona, Domain-wall motion driven by Laplace pressure in Co-Fe-B/MgO nanodots with perpendicular anisotropy, Phys. Rev. Applied 9, 064027 (2018)

[51] M. Karder, Dynamic scaling phenomena in growth processes, Physica B: Cond. Mater. **221**, 60-64 (1996).

[52] D. A. Huse, and C. L. Henley, Pinning and roughening of domain walls in Ising systems due to random impurities, Phys. Rev. Lett. **54**, 2708 (1985).

[53] G. Blatter, M. V. Feigel'man, V. B. Geshkenbein, A. I. Larkin, and V. M. Vinokur, Vortices in high-temperature superconductors, Rev. Mod. Phys. **66**, 1125 (1994).

[54] T. Shibauchi, L. Krusin-Elabum, V. M. Vinokur, B. Argyle, D. Weller, and B. D. Terris, Deroughening of a 1D domain wall in an ultrathin magnetic film by a correlated defect, Phys. Rev. Lett. **87**, 267201 (2001).

[55] F. Caysool, D. Ravelosona, C. Chappert, J. Ferré, and J. P. Jamet, Domain wall creep in magnetic wires, Phys. Rev. Lett. **92**, 107202 (2004).

Author's Biography

Ji-Sung Yu

TMNL., 23-410, Department of Physics and Astronomy, Seoul National University,
Gwanak-ro 1, Gwnak-gu, Seoul, 151-747, Republic of Korea
Phone : +82-2-884-9254 Fax : +82-2-884-9254
E-mail : noise@snu.ac.kr

Education

2010. 03. ~ 2012. 02. Kyeongbuk Science High School

2012. 03. ~ 2016. 08. Korea University **B.S.** in Physics

2017. 03. ~ 2023. 08. Seoul National University **Ph.D.** in Physics

Publications

1. **Ji-Sung Yu**, Seong-Hyub Lee, Minhwan Kim, Jiho Shin, Wooyoung Shim, and Sug-Bong Choe, Thickness dependence of creep-scaling behavior in Pt/Co single interface films, Journal of Magnetics. ??, Accepted (2023).

2. **Ji-Sung Yu**, Dae-Yun,Kim, Tae-Yun Kim, Seong-Hyub Lee, Jun-Young Chang, Minhwan Kim, Jaesung Yoon, Wooyoung Shim, Duck-Ho Kim, Cheol-Hwan Park, and Sug-Bong Choe, Exploring Dzyaloshinskii-Moriya interaction at single interface through in-vacuum MOKE and its correlation with lattice constant, Manuscript in preparation (2023).

3. **Ji-Sung Yu**, Tae-Yun Kim, Seong-Hyub Lee, Dae-Yun Kim, Minhwan Kim, Jiho Shin, Wooyoung Shim, Duck-Ho Kim, Cheol-Hwan Park, and Sug-Bong Choe, Chiral magnetic ordering at growing interface, Manuscript in preparation (2023).

4. **Ji-Sung Yu**, Seong-Hyub Lee, Minhwan Kim, Jiho Shin, Wooyoung Shim, Duck-Ho Kim, and Sug-Bong Choe, Interfacial Dzyaloshinskii-Moriya interaction within the scope of electron attraction in metallic magnetic films, Manuscript in preparation (2023).

5. **Ji-Sung Yu**, Dae-Yun Kim, Joon Moon, Seong-Hyub Lee, Jun-Young Chang, Duck-Ho Kim, Byoung-Chul Min, and Sug-Bong Choe, Chirality dependent roughness of magnetic domain walls, Appl. Phys. Lett. 121, 172403 (2022).

6. Yune-Seok Nam, Dae-Yun Kim, Yong-Keun Park, **Ji-Sung Yu**, Seong-Hyub Lee,

Duck-Ho Kim, Byoung-Chul Min, and Sug-Bong Choe, Exchange stiffness measurement scheme based on domain-wall chirality transition, Appl. Phys. Lett. 121, 072403 (2022).

7. Joon Moon, Seong-Hyub Lee, Kitae Kim, Jung-Hyun Park, Jun-Young Chang, **Ji-Sung Yu**, and Sug-Bong Choe, Method to check sample reproducibility by measuring magnetic domain wall motion in perpendicular magnetic anisotropy thin films, Journal of the Korean Magnetics Society. 31(5), 225-228 (2021).

8. Dae-Yun Kim, Min-Ho Park, Young-Keun Park, **Ji-Sung Yu**, Joo-Sung Kim, Duck-Ho Kim, Byoung-Chul Min, and Sug-Bong Choe, Huge domain-wall speed variation with respect to ferromagnetic layer thickness in ferromagnetic Pt/Co/TiO2/Pt films, Appl. Phys. Lett. 112, 062406 (2018).

Presentations

1. "Under Pt-Layer Thickness Dependence of the Dzyaloshinskii-Moriya Interaction in Pt/Co/Pt Films.", 10th International Symposium on Metallic Multilayers, Madrid, Spain, 2019. —*poster*
2. "Under Pt-Layer Thickness Dependence of the Dzyaloshinskii-Moriya Interaction in Pt/Co/Pt Films.", 11th International Conference on Magnetic and Superconducting Materials, Seoul, Korea, 2019. —*poster*
3. "Under Pt-Layer Thickness Dependence of the Dzyaloshinskii-Moriya Interaction in Pt/Co/Pt Films.", Samsung Global Research Symposium on Spin-Orbit Coupling Effects in Magnetic Nanostructures, Seoul, Korea, 2019. —*poster*
4. "Manipulation of Magnetic Anisotropy by Pt Under-Layer Thickness in Pt/Co/Pt Films", 11th International Conference on Advanced Materials and Devices, Jeju, Korea, 2019. —*poster*
5. "Manipulation of Magnetic Anisotropy by Pt Under-Layer Thickness in Pt/Co/Pt Films", 64th annual conference on Magnetism & Magnetic Materials, Las Vegas, USA, 2019. —*poster*
6. "Domain-wall-roughness-based determination scheme for Dzyaloshinskii-Moriya interaction", Korean Physical Society 2020 Fall Meeting, Virtual Conference, Korea, 2020. —*poster*
7. "Determination scheme for DMI based on chiral domain wall roughness measurement", Korean Magnetic Society 2020 winter conference, Yeosu, Korea,

2020. ─*poster*

8. "Measurement of Dzyaloshinskii-Moriya Interaction in Pt/Co Single Interface", 12th International Conference on Advanced Materials and Devices, Jeju, Korea, 2021. ─*poster*
9. "In-Situ Measurement of Single Interface Dzyaloshinskii-Moriya Interaction, Korean Magnetic Society 2021 winter conference, Gangneung, Korea, 2021. ─*poster*
10. "Measurement of Dzyaloshinskii-Moriya Interaction at Pt/Co Single Interface", 24th International Colloquium on Magnetic Films and Surfaces, Okinawa, Japan, 2022. ─*poster*
11. "Co Layer-Resolved Measurement of Dzyaloshinskii-Moriya Interaction at Pt/Co Single Interface", 67th annual conference on Magnetism & Magnetic Materials, Minneapolis, USA, 2022. ─*poster*
12. "Creep-scaling Behavior in Pt/Co Single Interface Films", 11th International Symposium on Metallic Multilayers, Seoul, Korea, 2023. ─*poster*
13. "Thickness dependence of creep-scaling behavior in Pt/Co single interface films", Korean Physical Society 2023 Spring Meeting, Daejeon, Korea, 2023. ─*oral*
14. "Correlation between magnetic susceptibility and interfacial Dzyaloshinskii-Moriya interaction in Pt/Co/X films", Korean Magnetic Society 2023 summer conference, Jeju, Korea, 2023. ─*oral*
15. "Thickness dependence of creep-scaling behavior in Pt/Co single interface films", IEEE International Magnetic Conference 2023, Sendai, Japan, 2023. ─*oral*
16. "Interfacial Dzyaloshinskii-Moriya interaction within the scope of electron

attraction in metallic films", 6th International Conference of Asian Union of Magnetics Societies, Bali, Indonesia, 2023. ─*oral*

국문 초록

잘로신스키-모리야 상호작용(DMI)은 스핀트로닉스 분야에서 중요한 요소로 부상하여, 카이랄 도메인월과 스커미온과 같은 카이랄 객체를 안정화하는데 중요한 역할을 한다. 차세대 메모리-로직 장치에 유망한 응용 가능성과 학술적 중요성 때문에, DMI에 대한 광범위한 연구와 탐구가 진행되고 있다. 그러나 DMI의 정확한 기저 메커니즘은 아직 논의중인 주제이다.

DMI의 발생에 대해 폭넓게 받아들여지는 설명은 구조적 반전 비대칭성 (Structural Inversion Asymmetry, SIA)에 의해 주도되는 계면에서의 전도전자의 스핀-궤도 상호작용에 기인한다는 것인데, 이는 DMI가 본질적으로 인터페이스 효과이며, 이의 기저 메커니즘을 해결하기 위해 인터페이스에 대한 포괄적인 이해가 필수적이다.

그러나 DMI를 조사하기 위한 기존의 실험적 접근 방법은, 주로 다중 인터페이스를 갖는 시스템을 기반으로 하고 있다. 이는 자성층에 불필요한 산화를 방지하기 위해 사용되는 보호층 등의 존재 때문인데, 이로 인해 현재의 실험적 접근 방법은 인터페이스에서의 DMI의 개별 기여를 분석하는데 한계가 있어, DMI에 대한 보다 깊은 이해를 어렵게 만들고 있다.

따라서, 우리는 단일 인터페이스에서 DMI의 개별 기여를 직접적인 관찰을 통해 해결할 수 있는 보다 원초적인 실험적 접근 방법을 제안한

다. 이 방법은 기존의 방법보다 더 명확하고 포괄적인 DMI에 대한 조사를 제공하여, DMI에 대한 깊은 이해를 도모한다.

1장에서는 DMI의 메커니즘에 대한 역사적인 개요를 소개하고, 수직 자기 이방성 (PMA)를 나타내는 기본적인 강자성체 시스템에 대하여 탐구하며, DMI 연구에 사용된 측정 방법을 소개한다. 이 장을 걸쳐서 강자성 박막에서 도메인 월 (DW)의 기본적 역학을 소개한다.

2장에서는 In−vacuum MOKE 시스템이라는 새로운 실험장치를 소개한다. 이 장치를 통해 단일 인터페이스에서 DMI를 관찰할 수 있는데, In−vacuum MOKE 시스템을 통한 DMI에 대한 연구는 1장에서 소개된 측정 방법을 기반으로 진행한다. 이 장에서는 주로 이 새로운 실험장치를 제작하고, 이를 이용하여 단일 인터페이스 구조 (Pt/Co)에서 DW 역학을 확인하는 것에 초점을 두고 있다. 이 장에서 얻은 결과는 단일 인터페이스 구조에서 DW 역학을 검증한 의미 있는 성과를 보여준다.

3장에서는 Pt/Co 단일 인터페이스에서 자성층 (Co)의 두께를 변화시킴으로써 DMI를 체계적으로 조사한다. 이 연구 결과는 DMI의 인터페이스 효과 특성을 확인하며, 더 나아가, 우리의 실험 장치의 신뢰성과 정확성을 입증하며, 아주 작은 원자 규모 두께까지 정밀한 제어와 감지를 할 수 있다는 것을 확인한다.

4장에서는 3장과 유사한 접근 방식을 따라, Pt/Co 단일 인터페이스에서 비자성층 (Pt)의 두께를 변화시키며 DMI를 체계적으로 조사한다.

재미있는 점은, 이론적 예상과는 대조적으로, 비자성층 두께에 따른 DMI의 강한 의존성이 관측되는데, X-선 회절 (XRD)를 통한 체계적인 검사를 통해, DMI와 Pt의 격자상수 간에 강한 상관관계가 있음을 발견한다. 이는 제일원리 연구를 통해 추가적으로 검증받는다. 이 상관관계를 활용하여, 시스템의 카이랄성을 조작하는 방법을 제안하고 보여준다. 3장과 4장에서 Pt/Co 단일 인터페이스에서 자성층과 비자성층의 두께 의존성을 철저히 조사함으로써, Pt/Co 인터페이스에서의 DMI에 대한 포괄적인 이해를 이룬다.

5장에서는 이전 장들에서 확립된 Pt/Co 인터페이스의 DMI에 대한 향상된 이해를 바탕으로, 다양한 물질들에서 DMI의 발생을 체계적으로 조사한다. 이는 우리가 앞서 설계한 첨단 In-vacuum MOKE 시스템의 활용을 기반으로 이루어진다. 이 연구에서는, Al, Cu, Nb, Pd, Hf, Ta와 같은 다양한 물질들을 Co위에 점진적으로, 원자 레벨의 두께로 증착하여 Pt/Co/X 구조를 만들어 가며 DMI를 체계적으로 탐구한다. 이를 통해, 다양한 물질들에 대한 DMI의 원자층별 기여를 정량화 한다. 또한, 이를 통하여 DMI의 발생에 중요한 역할을 하는, 일반적인 인터페이스의 길이가 존재함을 밝혀내며, 이러한 발견은 DMI의 인터페이스 특성에 대한 새로운 시야를 제공함과 동시에 발생의 기저 메커니즘에 대한 통찰력을 제공한다.

6장에서는 약한 PMA 시스템의 경우를 대비하여 DMI 조사를 위해

설계된 새로운 측정 방법을 소개한다. 이전 장들에서는 비교적 강한 PMA 조건에서 DMI에 대한 연구가 진행되었으며, 이는 명확한 DW 모션을 관측함을 기반으로 정확한 DW 속도 측정이 가능했기 때문이다. 그러나, 약한 PMA 시스템에서는, DW 모션을 정확하게 관측하는 것에 어려움이 생길 수 있어, DMI를 정확하게 측정하기에 어려움이 있을 수 있다. 이 장에서는, DW의 거칠기 측정을 기반으로, DMI를 측정하는 새로운 방법을 제안하며, 이 측정 방법은 DW 모션을 기반으로 한 DMI 측정에서 나타날 수 있는 어려움에 대한 해결책을 제시한다.

마지막장에서는 본 연구에서 제시한 결과의 결론과 전망을 다룬다. 이 연구의 주요 포인트는, Co/X 단일 인터페이스에서 DMI를 관찰함으로써 이루어졌는데, 이 선구적인 결과는 DMI 분야를 크게 발전시킬 것이며, 이 현상에 대한 명확한 탐지와 깊이 있는 분석을 제공한다.

키워드: 잘로신스키-모리야 상호작용, 계면, 도메인 월, 수직 자기 이방성, 자기광 커 효과, 카이랄성

학번: 2017-20880